Journal of Materials Science: Materials in Medicine

Impact of Cobalt and Chromium Concentrations on Bioapatite Lattice Stability and Mechanical Integrity

--Manuscript Draft--

Manuscript Number:	JMSM-D-26-00043R1
Full Title:	Impact of Cobalt and Chromium Concentrations on Bioapatite Lattice Stability and Mechanical Integrity
Article Type:	Original Research
Corresponding Author:	Alix Deymier University of Connecticut Health Center Farmington, CT UNITED STATES OF AMERICA
Corresponding Author Secondary Information:	
Corresponding Author's Institution:	University of Connecticut Health Center
Corresponding Author's Secondary Institution:	
First Author:	Kennedy Drake
First Author Secondary Information:	
Order of Authors:	Kennedy Drake
	Abigail Eaton
	Abiodun Aderibigbe
	Christina Krywka
	Arun Nair
	Alix Deymier
Order of Authors Secondary Information:	
Funding Information:	Division of Materials Research (107141) — Prof. Alix Deymier Division of Materials Research (2434467) — Dr. Arun Nair University of Connecticut Health Center (YIIP) — Ms. Kennedy Drake
Abstract:	This study explores how cobalt (Co) and chromium (Cr) ions, commonly released from metal-on-metal hip implants, can substitute into the bioapatite lattice of bone, potentially altering its structural and mechanical properties. The research utilizes biomimetic synthesis, spectroscopic analysis, elemental quantification, and both experimental and computational modeling to investigate how varying concentrations of these ions impact bioapatite's crystallinity, carbonate content, and elasticity. Findings aim to clarify the mechanisms by which Co and Cr incorporation affect bone mineral integrity and to inform strategies for mitigating adverse outcomes associated with metal ion release from orthopedic implants.
Response to Reviewers:	Response to Reviewers: (The response to reviewers is also included as supplementary material so that tables and images can be seen by the reviewers.) Reviewer #1: 1.The statement "7.04% of the 20% were substituted in the Co-containing apatite samples" is ambiguous and potentially inconsistent with Figure 1A, which appears to indicate approximately 50% incorporation efficiency. It is unclear whether "20%" refers to the initial solution composition or the targeted Ca-site substitution. The authors should clearly define this reference and reconcile the numerical discrepancy with the figure. Reporting substitution efficiency explicitly relative to the intended target would

Powered by Editorial Manager® and ProduXion Manager® from Aries Systems Corporation

greatly improve clarity.

We thank the reviewer for identifying this ambiguity. The ratios of the calcium nitrate, ammonium phosphate, chromium nitrate, cobalt nitrate, and sodium bicarbonate were selected such that if there was 100% formation efficiency the stoichiometry of the resulting powders would have 5 wt%, 10 wt%, or 20 wt% Co or Cr. As has been well established in the literature, these aqueous precipitation techniques are not 100% efficient and substitutions are rarely stoichiometric compared to the initial input values [1]. In the manuscript and in Figure 1A we show the predicted cation content (5, 10, 20 wt%) on the x-axis and the experimentally measured cation content (via ICP-OES) on the y-axis. Therefore, we can see that when we input solution concentrations that were stoichiometrically predicted to result in 5 wt% Cr/Co we only saw 2.67 wt% Co/Cr incorporation experimentally. In other words, about 50% of the expected cationic substitutions were actually incorporated into the apatite. This is also generally true for the other concentrations.
The methods have been updated to clarify this point and now read:
“Nominal metal loadings of 5, 10, and 20 wt% were prepared for both the Co and Cr series. For each synthesis, 23.62 g of calcium nitrate tetrahydrate was dissolved in deionized water. The cobalt-containing syntheses used 2.655, 5.314, or 10.628 g of $Co(NO_3)_2 \cdot 6H_2O$, while the chromium-containing syntheses used 2.001, 4.006, or 8.008 g of $Cr(NO_3)_3 \cdot 9H_2O$ for the nominal 5, 10, and 20 wt% formulations, respectively.
The phosphate and calcium/metal solutions were added dropwise to a solution of 0.420 M sodium bicarbonate (NaHCO3, Acros Organics). The temperature was maintained at approximately 65°C, and the pH was kept at 9.0 ± 0.5 using 1 M sodium hydroxide (NaOH, Acros, 98%). All water used in the synthesis was doubly deionized Milli-Q (18 MΩ) water to minimize the amount of fluoride present. After titration, the suspension was digested for two hours, cooled to room temperature, filtered, and the resulting precipitate was dried overnight at 60°C.
Because the efficiency of metal incorporation during apatite formation differs between Co and Cr, the actual incorporated metal concentrations differed from the nominal precursor formulations, Fig 1A. Therefore, all compositional analyses and discussion throughout this work are based on the measured Co and Cr concentrations determined by ICP-OES rather than the nominal precursor compositions.”

2.The manuscript lacks adequate statistical rigor throughout the results section. Although error bars are shown in several figures, their meaning is not defined, and no information is provided regarding sample size or statistical significance. The authors should define the error bars in all figure captions (e.g., standard deviation or standard error), report the number of replicates for each measurement, and include appropriate statistical analyses (such as ANOVA with post-hoc comparisons where relevant). Without this information, the reliability of the observed trends remains uncertain.

A single large batch of each of the 2.67%, 4.61%, and 7.04% Co-apatites and 2.67%, 4.61%, and 6.70% Cr-apatites was made for this study. This was done due to the difficulty in making consistent repeat batches of substituted apatites [1]. Preparing a single batch for each composition also allowed all chemical, structural, and mechanical characterizations to be performed on aliquots of the same material, enabling direct correlation between the different measurements.
For ICP-OES a single aliquot of each bioapatite was sent for analysis at Galbraith labs and therefore no error bars are shown. For FTIR, a single low-absorbance and a single high-absorbance pellet was made for each bioapatite. The error bars in Figure 2 are the standard error of the peak area fit as reported by OriginPro. This has been added to the caption of Figure 2. For XPS, a single aliquot was tested for each batch of bioapatites and therefore no error bars are shown. For EDX, 3 measurements were made on each aliquot of bioapatite. The error bars are standard deviations of those three measurements taken for each bioapatite sample. This has been added to the Figure 3 caption. For the mechanical testing, we were able to perform mechanical loading tests on 2 aliquots from each bioapatite sample. Therefore, the error bars in Figures 4, 5, 6, are standard deviations of these two measurements for each sample. This has been added to those respective captions. The error bars in Fig 7 represent the standard deviation of the 10,000 Monte Carlo simulations used in the compliance tensor optimization. This has been added to the caption of Fig. 7. Because only one synthesis batch was prepared for each composition, statistical comparisons (e.g., ANOVA) between compositions would constitute pseudoreplication, as the

measurements do not represent independent material syntheses. Accordingly, we have not performed inferential statistical analyses and instead interpret the results as compositional and structural trends. This limitation has been clarified in the revised manuscript.

3.The limitations of the DFT modeling are not sufficiently discussed. In particular, the exclusion of labile (surface) carbonate due to the use of periodic bulk models represents a significant simplification, especially given the nanocrystalline nature of bioapatite. While this is briefly mentioned, it should be explicitly addressed in the Discussion section, with a clear statement that the model captures bulk behavior only. The authors should also discuss how this limitation may contribute to discrepancies between experimental and computational results.

We thank the reviewer for their recommendation and insight. Due to modeling of only the bulk apatite crystals and the lack of inclusion of labile carbonate in the computational models, there is small difference between simulation predictions and experimental results. Differences between the experimental and computational lattice spacings have been included in Table S6 of the supplemental materials. The maximum a-axis spacing error is ~2.2% for the apatite with ~7-9wt% Co, and the maximum c-axis spacing error is ~0.4% for the apatites with ~3wt% Co and ~3wt% Cr. To address this in the manuscript, we've added the following discussion to section 3.4:

"The computational apatite models are used to predict the bulk properties of apatites, but the surface effects are not included in the fully periodic DFT calculations. Thus, the contribution of labile carbonate to the structural and mechanical properties observed in experimental apatite samples is not fully captured in the computational models. The maximum a-axis spacing difference between the experimental and computational apatites is ~2.2% with ~7-9wt% Co substitution. The maximum c-axis spacing difference is ~0.4% for the apatites with ~3wt% Co and ~3wt% Cr. Labile carbonate exclusion in the computational models may be a source of these minor differences between the experimental and DFT findings."

4.The choice of initial solution concentrations (0.288 M Co and 0.125 M Cr) is not adequately justified. It is unclear how these values relate to the intended substitution levels within the apatite lattice. The authors should explicitly state the target Ca^{2+} substitution percentages and explain how the chosen precursor concentrations were designed to achieve them.

We thank the reviewer for this helpful comment. We agree that the relationship between the precursor concentration and the intended metal-ion substitution levels was not sufficiently described in the original manuscript. In the original Methods, the stock solution concentrations (0.288 M Co and 0.125 M Cr) were reported, but these values are less informative than the actual precursor masses used during synthesis. We have therefore revised the Methods (see Response to Question 1) to report the masses of all reagents used for each nominal formulation rather than the stock solution concentrations. This provides a more direct and reproducible description of the synthesis procedure.
To further improve clarity, we have added Supplementary Table S1, which summarizes the precursor masses used for each nominal Co and Cr formulation. The actual incorporated Co and Cr contents were subsequently determined by ICP-OES and are reported throughout the Results and Discussion.

5.In Section 2.4, the terms "low concentration spectra" and "high concentration spectra" are used without clear definition. It is not evident whether this refers to metal ion concentration or to absorbance normalization during FTIR measurements. The authors should clarify what is meant by "concentration" in this context and explain the rationale for using different absorbance levels (2.5 versus 1.0).

We thank the reviewer for identifying this ambiguity. The terms "low concentration" and "high concentration" referred to the amount of apatite present in the KBr pellets and the resulting absorbance levels during FT-IR analysis, rather than to the concentration of Co or Cr within the apatite samples. To avoid confusion, we revised the text to replace this terminology with "standard absorbance" and "high-absorbance" pellets. We further

clarified that pellets with an absorbance of approximately 1.0 at the v3 PO43- band were used for routine spectral acquisition, whereas higher-absorbance pellets (>2.0) were prepared to improve resolution of the v2 CO32-, v2 PO43-, and v4 PO43- vibrational domains through higher-resolution FT-IR measurements. The methods now read:
“Each sample was finely ground, blended with potassium bromide (KBr, Uvasol), and compressed into 7 mm diameter pellets. Two pellet preparations were used: standard absorbance pellets, prepared to yield an absorbance of approximately 1.0 at the maximum v3 PO43- vibration band, and high-absorbance pellets, prepared to yield an absorbance greater than 2.0 at the same band maximum. Standard absorbance spectra were collected over the 400 to 4000 cm-1 range using 64 scans at a resolution of 4 cm-1 to observe the v4 PO4, v3 CO3, and v1v3 PO4 vibration modes. High-absorbance spectra were acquired using 64 scans at a higher resolution of 2.0 cm-1 to improve the resolution of the v2 CO32-, v2 PO4 , and v4 PO4 vibrational domains.”

6.The applied pressure range of approximately 100-500 MPa used in the WAXS experiments is significantly higher than typical physiological loading conditions for bone, which are on the order of 10-50 MPa. The authors should justify the use of this pressure range, for example as an accelerated testing approach, and discuss any potential non-physiological or nonlinear deformation effects that may arise at these higher pressures.

We thank the reviewer for this important observation. We agree that the applied pressures exceed those typically experienced by bone under physiological loading. The elevated pressure range was intentionally selected to generate lattice strains that could be reliably resolved by wide-angle X-ray scattering (WAXS), thereby enabling comparison of the pressure-dependent mechanical response of the different substituted apatite compositions. At physiological stress levels, the resulting lattice strains would be close to the resolution limit of the diffraction measurements.
We have revised the Methods section to clarify this rationale. It now states:
“ The applied pressure range exceeds physiological stresses typically experienced by bone tissue. However, these elevated pressures were intentionally employed to generate measurable changes in apatite lattice parameters and enable comparison of the pressure-dependent mechanical response of the substituted apatites. Similar high-pressure diffraction approaches have been widely used to investigate the elastic compressibility and structural stability of apatite and other mineralized materials [8,9]. Furthermore, the stress-strain relationships remained linear over the applied loading range (Fig. S2), indicating that the materials remained within the elastic deformation regime and that no evidence of nonlinear or irreversible deformation was observed."

7.The statement that "the maximum lattice spacing difference between methods is minimal" is qualitative and should be supported with quantitative data. The authors should report the actual numerical differences between experimental and simulated lattice parameters (e.g., percentage differences along the a- and c-axes) to allow a proper assessment of agreement.

The sentence that that reviewer is referring to reads: “However, the maximum lattice spacing difference between methods for the 2.67-3wt% Cr apatite is minimal; there is only 0.4% difference of the c-axis and 1.4% of the a-axis.” Therefore, it appears that the percent differences along the a- and c- axis are quantitatively reported.

8.The manuscript refers to a "high percentage of labile carbonate" in certain samples, but does not provide quantitative values. The authors should report the actual fraction of labile carbonate and describe how it was determined from FTIR deconvolution.

We thank the reviewer for this helpful suggestion. We expanded the FT-IR methods section to more clearly describe the deconvolution procedure used to quantify A-type, B-type, and labile carbonate species. Specifically, we now state that the v2 CO32- deformation region was deconvoluted using characteristic peak positions for each carbonate environment, and that the fitted peak areas were normalized to the total carbonate peak area before being scaled by the total carbonate content determined from the v3 CO32- /v1v3 PO4 area ratio. We also revised the manuscript to explicitly state that the relative abundances of these carbonate species are presented in Figure 2:

Powered by Editorial Manager® and ProduXion Manager® from Aries Systems Corporation

	“To quantify the carbonate environments, the out-of-plane v2 CO_3^{2-} deformation region was deconvoluted using initial peak positions corresponding to A-type CO_3^{2-} (~880 cm-1), B-type CO_3^{2-} (~873 cm-1), and labile CO_3^{2-} - (~864 cm-1). The B-type CO_3^{2-} contribution was fit using a Lorentzian function, whereas all other bands were fit using Gaussian functions due to their broader peak distributions. The fitted peak areas associated with A-type, B-type, and labile carbonate were normalized to the total carbonate peak area within the v2 CO_3^{2-} domain. These normalized fractions were subsequently scaled by the total carbonate content of each apatite, determined from the v3 CO_3^{2-}/v1v3 PO_4 area ratio, to obtain the relative abundance of each carbonate species [2]. These analyses allowed us to confirm the presence of characteristic apatite phases and enabled quantification of the relative abundance of A-type, B-type, and labile carbonate species, as well as the apatitic and non-apatitic phosphate environments (Figure 2).” We also specifically mention the relative amount of labile carbonate in the text. For example: Page 16: “Lattice parameter variances may be due to presence of labile carbonate on the surface of the experimental apatite samples which represents ~30% of the CO_3^{2-} content (Fig 2) in most samples and is not included in the computational modeling of the unit cell.” Page 17: “This may be due to high percentage of labile carbonate (48% of the total carbonate, Fig 2B) in the 4.61wt% Cr apatite, which we have noted as a potential cause of variance between experimental and DFT findings.” 9.The manuscript states that Co substitutes into Ca(1) and Ca(2) sites without preference, but no quantitative evidence is provided. Since DFT calculations appear to have been performed to assess site energetics, the authors should report the energy differences between possible substitution sites. Providing numerical ΔE values would support the conclusion of negligible site preference. We thank the reviewer for their recommendation to include more discussion of Co substitution sites. During preliminary studies, we investigated the ground state energy of Co substitution at Ca(1) and Ca(2) sites in carbonated apatites with ~3wt% Co. During Ca(2) site substitution, we predict ~0.62eV variance between Co substitution in two different Ca(2) locations. Co substitutions of two different Ca(1) sites have a difference of ~0.12eV between Ca(1) locations. We find Co substitution energy is dependent on its location in the apatite, with higher variability during Ca(2) site substitution than Ca(1) site substitution. Apatites with Co substitution of Ca(2) sites can have an energy both higher and lower than apatites with Co substitution of Ca(1) sites. Thus, there is not a clear Ca(1) or Ca(2) substitution site preference in Co apatites with carbonate at low Co wt%. Due to site preference inconsistency with a single Co substitution (~3wt% Co), we predict energy differences between mixed site and single site substitutions in carbonated apatite with a higher Co concentration. We find an energy difference of 0.83meV between Co apatite with equivalent Ca(1) and Ca(2) substitutions and Co apatite with only Ca(1) substitutions. This difference is negligible; the ionic minimization DFT energy convergence threshold is ~1.4meV, which is higher than this difference in energy for each substitution site. Thus, it is likely that the Co substitution occurs in both Ca sites in the experimental apatite samples, which has also been reported previously [3]. Since there is not a clear Co substitution site preference, we use iterative testing to determine substitution locations in the DFT apatite model that result in lattice parameters similar to those of the experimental samples. To address this in the manuscript, we’ve added the following to section 2.8: “During preliminary study, we determined that carbonated apatites with Co substitution at Ca(1) or Ca(2) sites have minimal ground state energy difference between them. Furthermore, we compare apatites with a higher concentration of Co substituting only Ca(1) sites and mixed Ca(1) and Ca(2) sites and find an energy difference less than the ionic minimization energy convergence threshold (~1.4meV) of the DFT calculations. Thus, it is likely that Co substitution occurs in both Ca sites in the experimental apatite samples, which has also been reported previously [3].” 10.The reduction in PO_4^{3-} content is attributed to non-apatitic phosphate without a clear mechanistic explanation. The authors should clarify whether this effect could arise from metal-phosphate interactions, surface adsorption processes, or changes in nucleation and growth kinetics. A more detailed discussion distinguishing between possible

thermodynamic and kinetic mechanisms would strengthen interpretation.

We thank the reviewer for this insightful comment. We agree that the mechanism underlying the reduction in non-apatitic phosphate warrants further discussion. While the present study cannot distinguish the specific atomistic mechanism, our data provide some insight. If the observed phosphate loss resulted simply from elimination of the hydrated surface layer, we would expect a corresponding decrease in labile carbonate. However, the labile carbonate fraction remained relatively unchanged, suggesting that the hydrated surface layer persists while its phosphate composition is modified. This observation argues against simple surface loss or adsorption effects and instead suggests that Co and Cr alter phosphate incorporation or retention during apatite crystal growth and maturation. This interpretation is consistent with previous work demonstrating that Co^{2+} and Cr^{3+} modify hydroxyapatite crystal growth and crystallinity [4].
We have revised the Discussion to clarify this interpretation. It now states:
“The preferential reduction in non-apatitic phosphate without a corresponding decrease in labile carbonate suggests that Co and Cr do not simply eliminate the hydrated surface layer of the apatite crystals or increase their maturation. Instead, these findings indicate that the heavy metal ions selectively modify the phosphate chemistry within this hydrated layer. One possible explanation is that Co and Cr alter apatite crystal growth and maturation, resulting in reduced incorporation or retention of phosphate in non-apatitic environments while leaving the carbonate-rich surface layer largely intact. Previous studies have similarly demonstrated that Co^{2+} and Cr^{3+} modify hydroxyapatite crystal growth, producing changes in crystallite size, crystallinity, and lattice parameters [4]. Although the present data do not distinguish whether these effects arise from altered nucleation, crystal growth kinetics, or local metal-phosphate interactions, the collective evidence suggests that Co and Cr influence the evolution of the hydrated surface layer during apatite formation rather than simply adsorbing to the crystal surface.”
11.The charge compensation mechanism for Cr^{3+} substitution, involving the introduction of interstitial oxygen, is presented as an assumption in the DFT model but is not experimentally validated. The authors should clarify whether this mechanism is supported by XPS or EDX data, or explicitly state that it remains a modeling assumption.
It has been suggested that chromium substitutes into apatite either as chromate substituting for phosphate [5] or Cr3+ substituting for Ca2+. Our XPS results indicated that the Cr in our samples was primarily present as Cr3+ and not as Cr6+ expected with chromate substitutions of phosphate (Fig 3A). This interpretation is further supported by our unpublished DFT analyses of chromate-substituted apatites, which did not reproduce the experimentally measured lattice parameters or elastic properties. Once Cr3+ substitution for Ca2+ was established, charge compensation remained to be determined. The presence of interstitial oxygen for charge balancing of Cr substitutions has been indicated experimentally by EXAFS analysis of Cr3+ substituted apatites by Lima et al [6]. On the other hand, Carrera et al. had found using cathodoluminescence that oxygen vacancies could also be used for charge balancing in Cr3+ substituted apatites [7]. To identify which of these two mechanisms was most likely, EXD was performed to determine the oxygen content as a function of Cr substitutions. As mentioned in the text “To confirm whether charge balance was regulated via oxygen vacancies or addition of interstitial vacancies, EDX was performed on the Cr-containing samples to determine the relationship between Cr and oxygen. EDX results indicate that oxygen increases with increasing Cr content, Fig 3B, suggesting that the presence of interstitial oxygen is most likely correct as suggested by [6].”
Based on these experimental observations, we modeled Cr3+ substitution with interstitial oxygen using DFT. This model matched the experimental lattice parameters with excellent agreement (0.4% difference of the c-axis and 1.4% of the a-axis). The close agreement between the experimental and calculated lattice parameters indicates that the interstitial oxygen model provides a physically realistic description of the Cr-substituted apatites. Although these calculations do not constitute direct experimental proof of the exact charge-compensation mechanism, they support the conclusion that the interstitial oxygen model is more consistent with the available experimental observations than an oxygen-vacancy model.

12.There are noticeable discrepancies between DFT predictions and experimental

measurements of lattice parameters and elastic properties. These differences are discussed qualitatively, but not quantified. The authors should provide a systematic comparison, including percentage errors, and discuss possible sources of discrepancy such as model limitations, compositional simplifications, or experimental uncertainties.

We thank the reviewer for this helpful suggestion. We agree that a more quantitative comparison between the DFT predictions and the experimental measurements strengthens the manuscript. We have therefore added Supplementary Tables S6 and S7, which summarize the experimental and DFT-derived lattice parameters and elastic properties together with their corresponding percentage differences. These tables provide a systematic assessment of the agreement between computational predictions and experimental measurements.
We have also added error calculations and discussion of the DFT model limitations to the manuscript. We ask the reviewer to please refer to the response to Q3, which discusses limitations of the DFT models. This response also includes manuscript edits regarding these limitations as a potential source of error between computational and experimental findings. Error values for the experimental data have been clarified for all of the quantitative data. These uncertainties in determination of lattice parameters from diffraction, measured metal incorporation by ICP-OES, and the propagation of uncertainty through the WAXS-based mechanical analysis collectively contribute to quantitative differences between computational predictions and experimental observations. Nevertheless, the DFT models reproduce the experimentally observed trends in both lattice parameters and elastic behavior, supporting the proposed substitution mechanisms.

13.The Monte Carlo optimization procedure used to extract elastic constants requires further clarification. The method relies on DFT-derived initial guesses and an assumed standard deviation, but the sensitivity of the results to these assumptions is not discussed. The authors should provide information on uncertainty propagation and report confidence intervals or variability ranges for the optimized elastic constants.

We thank the reviewer for this helpful comment. In terms of the DFT-derived initial guesses and standard deviations, we clarified the before settling on a standard deviation of 1 GPa we tested the optimization with standard deviations of 1, 5, and 10 GPa to confirm that the results converged to similar values. This has been added to the Methods section 2.11. This has also been discussed in further detail in our other publications using this technique [8-11] which are also cited in the methods.
In terms of variability ranges for the optimized elastic constants, the error bars in Fig 7 represent the standard deviation of the 10,000 Monte Carlo simulations used in the compliance tensor optimization. This has been added to the caption of Fig. 7.

14.The manuscript includes a placeholder for a schematic figure and would benefit from a clear visual summary of the proposed mechanism linking metal-on-metal implants to ion release, incorporation into bioapatite, and resulting mechanical changes. Additionally, including representative Raman and EDX spectra in the Supplementary Information, as well as convergence tests for the DFT calculations, would improve reproducibility. A data availability statement is also recommended.
A summary figure has been added as figure 10.

Furthermore, we thank the reviewer for their suggestion to include convergence tests of the DFT parameters in the supplemental materials and have included them in table (Table S4) and graph (Figure S7) format. We also include a statement in the manuscript section 2.8 referring to their presence in the supplemental materials:

“…, which are included in the supplemental materials as Table S4 and Figure S7.”

Reviewer #3:
1.Clinical framing and introductory claims need correction. The introduction states that metal-on-metal implants were used in approximately one-third of U.S. THAs and cites a systemic cobaltism review. (replace or supplement this with FDA, registry, or orthopedic surveillance literature)
We thank the reviewer for this suggestion. We revised the introduction to improve the clinical framing of MoM implant utilization. Specifically, we removed the statement that MoM implants were used in approximately ⅓ of all U.S. THAs and replaced it with

epidemiologic data from orthopedic literature describing both global and U.S. adoption of MoM bearings. The revised text now highlights that more than one million MoM implants have been used worldwide and that MoM bearings accounted for approximately 35% of 112,095 primary THAs captured in a large U.S. arthroplasty database by 2006. We also expanded the discussion of the clinical rationale underlying MoM implant adoption, including reduced wear and improved stability associated with larger femoral head diameters. The beginning of the introduction now reads:
“Metal-on-Metal (MoM) hip implants gained widespread adoption in the late 20th and early 21st centuries due to several perceived advantages over traditional polyethylene or ceramic bearing surfaces. The hardness of the cobalt-chromium alloys was expected to reduce wear, while the use of larger femoral head diameters offered the potential for improved joint stability and a reduced risk of dislocation.[12-15]. Consequently, MoM articulations were increasingly utilized worldwide, with more than one million MoM hip implants estimated to have been implanted globally [16]. In the United States, MoM bearings accounted for approximately 32-40% of primary total hip arthroplasties (THA) and 26-32% of revision THAs between 2005 and 2010, with utilization peaking in 2008. An estimated 755,000 patients in the United States received MoM bearings between 2000 and 2010, the majority during primary total hip arthroplasty (THA) procedures[17].
According to the FDA, MoM hip implants are typically composed of cobalt-chromium metal alloys, including a metal femoral head (metal head), femoral stem in the thighbone (metal stem), and metal acetabular component (metal cup). Although these devices were introduced to improve implant longevity and stability, mechanical wear and corrosion at the articulating surfaces can result in the release of cobalt (Co) and chromium (Cr) ions into the acetabulofemoral joint. These ions may accumulate in periprosthetic tissues, enter systemic circulation, and contribute to local and systemic adverse effects, including compromised bone health and an increased risk of fracture [18].”

2.Phase purity and true substitution are insufficiently demonstrated at least one of: Rietveld refinement, high-resolution XRD comparison to secondary phases, TEM/SAED, EXAFS/XANES, PDF analysis, or strong XPS/WAXS/FTIR deconvolution evidence showing absence of secondary phases (otherwise state it in limitations).
We thank the reviewer for this important suggestion. To further assess phase purity, we performed full-pattern Rietveld refinements on the 5, 10, and 20 wt% Cr-substituted and Co-substituted apatite compositions using BGMN via the Profex program [19]. In addition to the carbonated apatite structural model, several candidate crystalline secondary phases that could reasonably form during synthesis were systematically evaluated, including calcite, octacalcium phosphate (OCP), cobalt hydroxide, cobalt bishydrogen phosphate dihydroxide, chromium phosphate (α-$CrPO_4$), and guyanaite. For all six compositions, the diffraction patterns were well described by the carbonated apatite structural model, yielding excellent agreement between the calculated and experimental diffraction patterns (weighted profile residuals, Rwp = 1.45–4.59%, $\chi^2 \approx$ 1.0–1.4). Candidate chromium- and cobalt-containing secondary phases consistently refined to zero or negligible phase fractions and did not produce meaningful improvements in the refinement statistics. Specifically, α-$CrPO_4$ and guyanaite refined to zero or trace amounts (<0.2 wt%) and either did not improve or slightly worsened the fit. Likewise, cobalt hydroxide refined to zero for all compositions, while cobalt bishydrogen phosphate dihydroxide refined to negligible amounts (<0.3 wt%) without improving the refinements. Trace amounts of calcite were occasionally obtained during refinement (generally <1 wt%, with a maximum apparent fraction of approximately 2.7 wt% for the 20 wt% Co sample); however, these yielded little or no improvement in the overall fit and were therefore not considered compelling evidence for a discrete crystalline calcite impurity. OCP was also evaluated because of its structural similarity to apatite. Although non-zero OCP phase fractions were obtained in some refinements, inclusion of this phase generally did not improve—and in several cases slightly worsened—the refinement statistics. Given the substantial diffraction overlap between OCP and poorly crystalline apatite, these refinements were not interpreted as evidence for a separate crystalline OCP phase.
Overall, the Rietveld refinements indicate that the diffraction patterns are consistent with substituted carbonated apatite as the dominant crystalline phase, with no detectable crystalline chromium- or cobalt-containing secondary phases within the detection limits of laboratory X-ray diffraction. The fitting details have been added as a supplemental table, Table S3.

These findings are also consistent with our XPS results, which identify chromium in the Cr^{3+} oxidation state rather than as chromate species, and with the systematic changes in lattice parameters observed by XRD, providing complementary evidence that the transition-metal ions are incorporated into the apatite structure rather than forming detectable crystalline secondary phases.
We have added these results to the manuscript. In the methods section we've added:
"Lab X-ray Diffraction and Rietveld Refinement
Powder X-ray diffraction (XRD) patterns were collected at room temperature using Bruker D2 Phaser Diffractometer equipped with Cu Kα radiation (λ = 1.5406 Å) operating at 30 kV and 10 mA with an acquisition time of 1.0 s/increment and an increment of 0.02o ranging from 20 to 60° (2θ). XRD spectra for all samples are show in Fig. S2.
Rietveld refinements were performed using BGMN version 4.2.22 with the graphical interface Profex. A carbonated apatite structural model was used as the primary phase for all refinements. Background, scale factor, zero shift, lattice parameters, peak profile parameters, crystallite size/strain parameters (where applicable), and atomic displacement parameters were refined following convergence of the model. Candidate secondary phases were evaluated individually by adding them to the refinement while maintaining the carbonated apatite phase. Phases considered included calcite, octacalcium phosphate (OCP), α-chromium phosphate (α-$CrPO_4$), guyanaite, cobalt hydroxide, and cobalt bishydrogen phosphate dihydroxide. Refinement quality was assessed using the weighted profile residual (Rwp), expected residual (Rexp), goodness-of-fit (χ^2), and inspection of the observed, calculated, and difference diffraction patterns."
In the results section:
"Rietveld refinement was performed for the 5, 10, and 20 wt% Cr- and Co-substituted apatite compositions using a carbonated apatite structural model. Good agreement between the calculated and experimental diffraction patterns was obtained for all samples (Rwp = 1.45–4.59%, χ^2 = 1.0–1.4). Candidate secondary phases, including calcite, α-$CrPO_4$, guyanaite, cobalt hydroxide, cobalt bishydrogen phosphate dihydroxide, and octacalcium phosphate (OCP), were also evaluated. Chromium- and cobalt-containing secondary phases refined to zero or negligible phase fractions. Complete refinement statistics and phase fractions are provided in Table S3."
3.Oxygen charge-compensation mechanism is overinterpreted. The manuscript's Cr model assumes Cr^{3+} substitution at Ca(2) with interstitial oxygen based partly on EDX oxygen increase. EDX oxygen quantification in light-element, porous powders mounted on carbon tape and coated with Au-Pd is not sufficiently quantitative to justify a 1:1 Cr:O interstitial model by itself.(as far as i know please check) i suggest charge-balanced formulae for each composition.
We thank the reviewer for this important comment. We agree that SEM-EDX is not sufficiently quantitative to determine the absolute oxygen stoichiometry or to establish a precise 1:1 Cr:O charge-compensation ratio.
Our intent was not to use EDX to determine the exact oxygen content, but rather to evaluate whether oxygen content exhibited a systematic increase or decrease with increasing chromium substitution to determine possible charge balance mechanisms (See answer to Reviewer1 Q9). While oxygen quantification by EDX has known limitations, the measured oxygen content increased consistently (approximately 6–10 at.%) with increasing Cr concentration. If charge compensation occurred predominantly through oxygen vacancies, the opposite trend would be expected. Thus, although EDX cannot directly prove the presence or stoichiometry of interstitial oxygen, the observed trend provides qualitative support for oxygen incorporation rather than oxygen loss. For this reason, the DFT calculations were performed using the interstitial oxygen model previously proposed by Lima et al. [5]. The close correlation between the experimental and theoretical lattice spacings providing additional support that this is the most plausible charge-compensation mechanism for the materials investigated.
Although the composition of the DFT models had been described for all of the Cr-substituted apatites in the methods, we have further included a supplemental table showing the formulae of all 3 DFT models of Cr3+ substitutions, Table S2, which is referenced in the text. Note that the DFT models use an orthorhombic cell which is a double hexagonal cell and therefore the starting formula for hydroxyapatite (HAP) is Ca20(PO4)12(OH)4.

4.DFT assumptions require stronger validation, several assumptions need justification: fixed carbonate content, exclusion of labile carbonate, fixed Cr substitution at Ca(2),

interstitial oxygen at 1:1 Cr:O, and absence of explicit testing of the minor Cr^{6+} population detected by XPS.

We thank the reviewer for their recommendation and insight. Carbonate content in the experimental apatite crystals is estimated to be 8.1-8.8wt% in the crystals for Co substitution and 9.9-12.1wt% in the crystals for Cr substitution. In the orthorhombic unit cell used for Co and Cr apatite modeling, substitution wt% is constrained by the number of potential substitution sites in the cell. It is computationally expensive to create apatite models large enough to exactly mimic the carbonate content in the experimental samples. However, we model the experimental samples within the limitations of DFT using exact substitutions of 8.8-9wt% carbonate in the Co apatites and 11.8-12.2wt% carbonate in the Cr apatites. These ranges are close to the experimental values and capture the carbonate content difference between apatites with Co and Cr substitutions. Moreover, the computational models are intended to capture the trend in the lattice and mechanical properties as the Co and Cr concentration increases. To address this in the manuscript, we've included the following in section 2.8:

"We developed apatite unit cells with CO32- wt% similar to the experimental samples such that their corresponding ratio of A:B-type carbonate substitution is same. Carbonate concentration is approximately constant in all Co apatite crystals (8.8-9wt%) and Cr apatite crystals (11.8-12.2wt%). These concentrations capture the carbonate content difference between the experimental Co and Cr apatite samples."

Our periodic bulk apatite models do not include surface effects such as labile carbonate. We address this DFT limitation as a potential source of minor error between computational and experimental findings in section 3.4 of the manuscript:

"The computational apatite models are used to predict the bulk properties of apatites, but the surface effects are not included in the fully periodic DFT calculations. Thus, the contribution of labile carbonate to the structural and mechanical properties observed in experimental apatite samples is not fully captured in the computational models. The maximum a-axis spacing difference between the experimental and computational apatites is ~2.2% with ~7-9wt% Co substitution. The maximum c-axis spacing difference is ~0.4% for the apatites with ~3wt% Co and ~3wt% Cr. Labile carbonate exclusion in the computational models may be a source of these minor differences between the experimental and DFT findings."

In addition to previous studies suggesting Cr substitutes Ca(2) sites [6, 7, 20, 21], we predict that Cr substitution of Ca(2) results in ~1.3eV lower energy than Ca(1) in carbonated apatite with interstitial oxygen. Due to this strong Ca(2) site preference, we only substitute Ca(2) sites with Cr ions. Furthermore, we only consider Cr3+ in the computational models and exclude Cr6+ due to its low concentration in the experimental Cr apatite samples and very low difference between the experimental and computational findings of lattice and mechanical properties. To address this in the manuscript, we've included the following in sections 2.8 and 3.4:

"The Cr substitution is performed by substituting Cr3+ for Ca2+ in the Ca(2) site near OH- channels based on parametric studies, experimental findings, and previous studies [6, 20-22]. During our preliminary study, we predict Cr3+ substitution of Ca(2) sites is ~1.3eV more favorable (lower) than Ca(1) sites. We exclude Cr6+ substitutions, which appear in the experimental apatite samples, due to very low concentration."
"When comparing the computational and experimental data of the lattice properties of Cr apatites, the low Cr6+ substitution content likely also causes a small difference between both results."

5.Crystallographic terminology and figure labels need correction. Figures and text repeatedly refer to "d-spacing" values that appear to be lattice parameters. For example, values near 6.9 Å and 9.3 Å correspond more closely to hydroxyapatite c and a lattice parameters, not the raw d-spacings of the (002) and (310) planes. The authors should explicitly show the conversion from measured peak positions to d-spacing and then to lattice parameter.

We thank the reviewer for this helpful observation. We agree that the original

manuscript did not clearly distinguish between the measured d-spacings and the derived hydroxyapatite lattice parameters. The methods section has been revised to explicitly describe the analysis workflow, whereby diffraction peak positions were first converted to d-spacings using Bragg's law and subsequently converted to the corresponding hydroxyapatite lattice parameters using the crystallographic relationships assuming a hexagonal unit cell. In addition, the text and Figure 5 have been revised to consistently refer to the reported values as lattice parameters where appropriate.

a.The FWHM axis in Figure 4 is labeled in radians with values as high as ~50, which is physically implausible if literal radians. The authors should correct the units and state whether FWHM is in pixels, detector units, q-width, degrees, milliradians, or reciprocal-space units.

We thank the reviewer for catching this error. The data had accidentally been posted in pixels. It has now been converted to radians.

6. Raman/Cr inconsistency should be resolved. The methods state that Raman was performed exclusively on Co-containing samples because Cr fluoresces under the 785 nm laser. Later, the text discusses Raman and FTIR carbonate ratios for both Co and Cr samples. The authors should clarify whether Raman data exist for Cr samples; if not, all statements implying Raman validation for Cr-containing apatites should be removed or revised.

We thank the reviewer for identifying this ambiguity. Raman spectroscopy was performed only on Co-containing apatites because chromium-containing samples exhibited fluorescence under the 785 nm excitation laser, preventing reliable Raman analysis. We have revised the Results and Discussion sections to explicitly distinguish between the analytical methods used for Co- and Cr-containing apatites. The revised text now clarifies that carbonate-to-phosphate ratios for Cr-containing apatites were determined using FTIR and ICP-OES/CHN analyses only, and any wording implying Raman validation of Cr-containing apatites has been removed.

7. Statistics and reproducibility are not yet adequate
The manuscript does not clearly state the number of independent synthesis batches per condition, number of ICP-OES/CHN repeats, XPS fitting reproducibility, FTIR/Raman deconvolution error, or WAXS loading replicates. Error bars are present in some figures, but the definition of error is not consistently stated. Readers will expect independent biological/material replicates or a clear justification for why technical replicates are sufficient.

See response to Reviewer 1 Question 2.

8. Presentation needs substantial polishing
The manuscript contains multiple wording, formatting, and typographical issues, including "as can been seen," "Youngs," "phosphorous" where "phosphorus" is intended, "metal-on metal," "that crystal lattice," inconsistent superscripts, inconsistent figure units, and equation-numbering gaps. The graphical abstract page appears cropped/low-resolution in the submitted PDF and should be replaced with a clean full-width version.

We thank the reviewer for their careful reading of the manuscript. We have thoroughly revised the manuscript to improve its overall presentation, including correcting typographical, grammatical, formatting, and terminology inconsistencies throughout the text. Examples include correcting wording (e.g., “as can been seen” to “as can be seen”), standardizing scientific terminology (e.g., “Young’s modulus”, “phosphorus”, and “metal-on-metal”), ensuring consistent use of superscripts, units, and figure formatting, and addressing equation numbering inconsistencies. In addition, the graphical abstract has been replaced with a higher-resolution, full-width version in the revised submission.

References:
1.Drouet, C., Apatite Formation: Why It May Not Work as Planned, and How to Conclusively Identify Apatite Compounds. BioMed Research International, 2013. 2013:

p. 12.
2.Ortali, C., et al., Consolidation of bone-like apatite bioceramics by spark plasma sintering of amorphous carbonated calcium phosphate at very low temperature. Journal of the European Ceramic Society, 2018. 38(4): p. 2098-2109.
3.Veselinović, L., et al., Crystal structure of cobalt-substituted calcium hydroxyapatite nanopowders prepared by hydrothermal processing. Journal of Applied Crystallography, 2010. 43: p. 320-327.
4.Mabilleau, G., et al., Cobalt, chromium and nickel affect hydroxyapatite crystal growth in vitro. Acta Biomater, 2010. 6(4): p. 1555-60.
5.Grisafe, D.A. and F.A. Hummel, Pentavalent ion substitutions in the apatite structure part A. Crystal chemistry. Journal of Solid State Chemistry, 1970. 2(2): p. 160-166.
6.Lima, T.A.R.M., et al., The incorporation of chromium (III) into hydroxyapatite crystals. Materials Letters, 2015. 140: p. 187-191.
7.Carrera, K., et al., Formation of Oxygen Vacancies in Cr3+-Doped Hydroxyapatite Nanofibers and Their Role in Generating Paramagnetism. Biomedical Materials & Devices, 2025. 3(1): p. 529-544.
8.Wingender, B., et al., Carbonate substitution significantly affects the structure and mechanics of carbonated apatites. Acta Biomaterialia, 2021. 122: p. 377-386.
9.Forien, J.-B., et al., X-ray diffraction and in situ pressurization of dentine apatite reveals nanocrystal modulus stiffening upon carbonate removal. Acta Biomaterialia, 2021. 120: p. 91-103.
10.Wong, S., et al., The location of cationic substitutions in carbonated biomimetic apatites significantly affects crystal nanomechanics. Sci Rep, 2024. 14(1): p. 22625.
11.Wong, S., et al., Increasing A-type CO32− substitution decreases the modulus of apatite nanocrystals. Journal of the Mechanical Behavior of Biomedical Materials, 2025. 166: p. 106962.
12.Triclot, P., Metal-on-metal: history, state of the art (2010). Int Orthop, 2011. 35(2): p. 201-6.
13.Rieker, C.B., R. Schön, and P. Köttig, Development and validation of a second-generation metal-on-metal bearing: laboratory studies and analysis of retrievals. J Arthroplasty, 2004. 19(8 Suppl 3): p. 5-11.
14.Rieker, C. and P. Kottig, In vivo tribological performance of 231 metal-on-metal hip articulations. Hip Int, 2002. 12(2): p. 73-76.
15.Davis, T.P., Metal-on-Metal Hip Arthroplasty: A Comprehensive Review of the Current Literature. Cureus, 2023. 15(11): p. e48238.
16.Matharu, V.K. and G.S. Matharu, Metal-on-metal hip replacements: implications for general practice. Br J Gen Pract, 2017. 67(665): p. 544-545.
17.Kurtz, S.M., et al., Prevalence of Metal-on-Metal Bearings in the United States, in Metal-On-Metal Total Hip Replacement Devices. 2013, ASTM International. p. 0.
18.Kovochich, M., et al., Understanding outcomes and toxicological aspects of second generation metal-on-metal hip implants: a state-of-the-art review. Crit Rev Toxicol, 2018. 48(10): p. 853-901.
19.Doebelin, N. and R. Kleeberg, Profex: a graphical user interface for the Rietveld refinement program BGMN. Journal of Applied Crystallograph...

Powered by Editorial Manager® and ProduXion Manager® from Aries Systems Corporation

Manuscript
Click here to access/download;Manuscript;260803_Co_Cr_Paper_MSE_MatM

Impact of Cobalt and Chromium Concentrations on Bioapatite Lattice Stability and Mechanical Integrity

Kennedy Drake[1], Abigail Eaton[2], Abiodun Aderibigbe[3], Christina Krywka[4], Arun Nair[5], Alix Deymier[6]

1. Dept of Biomedical Engineering, UConn Health, Farmington, CT, USA, ORCID: 0009-0002-9641-5317
2. Air Force Institute of Technology, Dayton, OH, USA, ORCID: 0009-0007-1700-3821
3. Dept of Materials Science and Engineering, University of Connecticut, Storrs, CT, USA, ORCID: 0000-0003-2379-669X
4. Helmholtz-Zentrum Hereon, Geesthacht, Germany, ORCID: 0000-0003-2940-3359
5. Air Force Institute of Technology, Dayton, OH, USA, ORCID: 0000-0003-2144-5335
6. Dept of Biomedical Engineering, UConn Health, Farmington, CT, USA, ORCID: 0000-0001-5187-4427

Corresponding Author:
Alix Deymier
ORCID: 0000-0001-5187-4427
deymier@uchc.edu
520-248-1956
860-679-8916

Abstract:

This study explores how cobalt (Co) and chromium (Cr) ions, commonly released from metal-on-metal hip implants, can substitute into the bioapatite lattice of bone, potentially altering its structural and mechanical properties. The research utilizes biomimetic synthesis, spectroscopic analysis, elemental quantification, and both experimental and computational modeling to investigate how varying concentrations of these ions impact bioapatite's crystallinity, carbonate content, and elasticity. Findings aim to clarify the mechanisms by which Co and Cr incorporation affect bone mineral integrity and to inform strategies for mitigating adverse outcomes associated with metal ion release from orthopedic implants.

Keywords: Apatite, Chromium, Cobalt, Substitutions, Bone mineral, Stiffness

Conflicts of interest: The authors have no relevant financial or non-financial interests to disclose.

Acknowledgements: This work was supported in part by the Institute of Materials Science at UConn, which provided access to central research facilities and instrumentation. We thank Sobhan Katebifar for collecting the EDX data at CAMMA at UConn. Measurements were performed at PETRA III at DESY (Hamburg, Germany), supported by the Helmholtz Association HGF. The authors gratefully acknowledge beam time on PO7 under proposal I-20231024 and the support of the beamline staff. Funding was provided by NSF grant 107141. KD was supported by the Young Innovative Investigator Program (YIIP) at UConn Health. AN and AE acknowledge support from NSF grant 2434467.

1 Introduction

Metal-on-Metal (MoM) hip implants gained widespread adoption in the late 20th and early 21st centuries due to several perceived advantages over traditional polyethylene or ceramic bearing surfaces. The hardness of the cobalt-chromium alloys was expected to reduce wear, while the use of larger femoral head diameters offered the potential for improved joint stability and a reduced risk of dislocation.[1-4]. Consequently, MoM articulations were increasingly utilized worldwide, with more than one million MoM hip implants estimated to have been implanted globally [5]. In the United States, MoM bearings accounted for approximately 32-40% of primary total hip arthroplasties (THA) and 26-32% of revision THAs between 2005 and 2010, with utilization peaking in 2008. An estimated 755,000 patients in the United States received MoM bearings between 2000 and 2010, the majority during primary total hip arthroplasty (THA) procedures[6].

According to the FDA, MoM hip implants are typically composed of cobalt-chromium metal alloys, including a metal femoral head (metal head), femoral stem in the thighbone (metal stem), and metal acetabular component (metal cup). Although these devices were introduced to improve implant longevity and stability, mechanical wear and corrosion at the articulating surfaces can result in the release of cobalt (Co) and chromium (Cr) ions into the acetabulofemoral joint. These ions may accumulate in periprosthetic tissues, enter systemic circulation, and contribute to local and systemic adverse effects, including compromised bone health and an increased risk of fracture [7].

The release of these metal ions has been associated with a range of adverse biological effects. Locally, the accumulation of metallic debris can provoke adverse local tissue reactions (ALTRs), including adverse reactions to metal debris and aseptic lymphocyte-dominated vasculitis-associated lesions [8]. These responses can lead to osteolysis, bone weakening, and implant loosening or failure [9, 10]. Systemically, elevated levels of Co and Cr have been linked to cardiovascular [11], neurological [12, 13], and renal complications [14]. While the immunological and cytotoxic mechanisms of metal ion exposure have been extensively studied, the physicochemical interactions between these ions and bone mineral remain less understood.

A growing body of evidence suggests that released metal ions may be directly incorporated into the mineral phase of bone or bioapatite [15]. Bioapatite is a nanocrystalline, carbonated form of hydroxyapatite, and it composes approximately 70 wt.% of bone. Hydroxyapatite and other apatite forms readily allow for both anionic (e.g., F^-, Cl^-, and CO_3^{2-}) and cationic (e.g., Mg^{2+}, Na^+, K^+, etc.) substitutions within their crystal structure [15]. Of these, carbonate substitutions are most prominent, accounting for nearly 2-8 wt.% of natural bone mineral [16]. The substitution of carbonate (CO_3^{2-}) into the crystal lattice primarily occurs as a

replacement for phosphate (PO_4^{3-}) groups, which is known as a B-type carbonate substitution. Alternately, CO_3^{2-} can also replace hydroxide (OH^-) groups, resulting in an A-type carbonate substitution. Furthermore, CO_3^{2-} may also reside in the non-apatitic surface layer of bioapatite crystals and is referred to as labile carbonate [17]. The carbonated form of apatite generally exhibits reduced crystallinity, smaller crystallite size, and lower stiffness, which are properties that align with the characteristics of native bone mineral [18, 19]. These carbonate substitution locations are therefore key in defining the mineral's solubility, crystallinity, mechanical performance, and other physical and chemical characteristics.

Similarly to carbonate, a wide range of other ions can be readily substituted into the bioapatite lattice. This can include, but is not limited to monovalent cations such as silver (Ag^+), sodium (Na^+), potassium (K^+), etc., bivalent cations such as magnesium (Mg^{2+}), strontium (Sr^{2+}), zinc (Zn^{2+}), barium (Ba^{2+}), etc., or multi-valent cations such as Co or Cr [20]. Most of these ions have been shown to substitute for calcium (Ca^{2+}) in the bioapatite lattice. Cationic substitutions have been shown to influence the positioning of carbonate ions; for example, the addition of K^+ has demonstrated a preference toward A-type carbonate substitutions [21]. These types of changes in the lattice and composition have also been shown to compromise the mineral stiffness, which is reduced [19, 21]. In theory, the presence and concentration of Co and Cr ions is expected to alter the crystal lattice, thus impacting the bioapatite's composition, solubility, and mechanical stiffness.

Given the established release of these heavy metal ions in patients with MoM implants and their similar ionic charges and radii compared to native Ca^{2+} (Co: 70 pm, Cr: 87 pm, Ca: 100 pm), it is plausible that these ions may also similarly substitute into bone mineral and influence the chemical composition, structural organization, and mechanical integrity of the mineral [22]. However, the precise mechanisms by which Co and Cr incorporate and alter the physical and mechanical properties of bioapatite are not understood. In this study, we investigate the incorporation of Co and Cr into the bioapatite lattice and evaluate the effects of these substitutions on the structural and mechanical properties of the material. Biomimetic apatites with varying concentrations of either Co or Cr were synthesized using a direct aqueous precipitation method. Spectroscopic techniques, including Fourier Transform Infrared Spectroscopy (FT-IR) and Raman spectroscopy, were used to assess crystallinity and carbonate content, including the presence and distribution of A-type, B-type, and labile carbonate (CO_3^{2-}) species. Elemental analyses via Inductively Coupled Plasma Optical Emission Spectroscopy (ICP-OES) and CHN analysis were used to quantify compositional incorporation. Mechanical properties were evaluated using synchrotron wide-angle X-ray scattering (WAXS) under hydrostatic compression to measure lattice strain and compute elastic

moduli.

We also utilize Density Functional Theory (DFT) based computational modeling to model the effects of ionic substitution on lattice elasticity, providing theoretical predictions of elastic constants and *lattice spacing* values across various substitution levels. These computational models help guide experimental data interpretation and informed optimization procedures to calculate the compliance tensor of the substituted lattices. Thus, the confluence of experimental and computational results offers detailed insight into how Co and Cr ions influence the structural and mechanical integrity of bioapatite. Understanding the behavior of these heavy metal ions in bone mineral is critical for evaluating the role of ionic substitution in MoM implant failure and for guiding future strategies to mitigate adverse outcomes associated with metal ion release.

2 Methods and Materials

2.1 Bioapatite Synthesis

Nanocrystalline bioapatite samples with varying concentrations of Co or Cr were synthesized via aqueous precipitation methods modified from [18-22]. Calcium nitrate tetrahydrate ($Ca(NO_3)_2 \cdot 4H_2O$, Thermo Scientific) and diammonium hydrogen phosphate ($(NH_4)_2HPO_4$, Thermo Scientific) were dissolved separately in deionized water. For the metal-substituted apatites, cobalt nitrate hexahydrate ($Co(NO_3)_2 \cdot 6H_2O$, Thermo Scientific) or chromium nitrate nonahydrate ($Cr(NO_3)_3 \cdot 9H_2O$, Thermo scientific) was added to the calcium precursor solution prior to precipitation.

Nominal metal loadings of 5, 10, and 20 wt% were prepared for both the Co and Cr series. For each synthesis, 23.62 g of calcium nitrate tetrahydrate was dissolved in deionized water. The cobalt-containing syntheses used 2.655, 5.314, or 10.628 g of $Co(NO_3)_2 \cdot 6H_2O$, while the chromium-containing syntheses used 2.001, 4.006, or 8.008 g of $Cr(NO_3)_3 \cdot 9H_2O$ for the nominal 5, 10, and 20 wt% formulations, respectively, Table S1.

The phosphate and calcium/metal solutions were added dropwise to a solution of 0.420 M sodium bicarbonate ($NaHCO_3$, Acros Organics). The temperature was maintained at approximately 65°C, and the pH was kept at 9.0 ± 0.5 using 1 M sodium hydroxide (NaOH, Acros, 98%). All water used in the synthesis was doubly deionized Milli-Q (18 MΩ) water to minimize the amount of fluoride present. After titration, the suspension was digested for two hours, cooled to room temperature, filtered, and the resulting precipitate was dried overnight at 60°C.

Because the efficiency of metal incorporation during apatite formation differs between Co and Cr, the actual incorporated metal concentrations differed from the nominal precursor

formulations, Fig 1A. Therefore, all compositional analyses and discussion throughout this work are based on the measured Co and Cr concentrations determined by ICP-OES rather than the nominal precursor compositions.

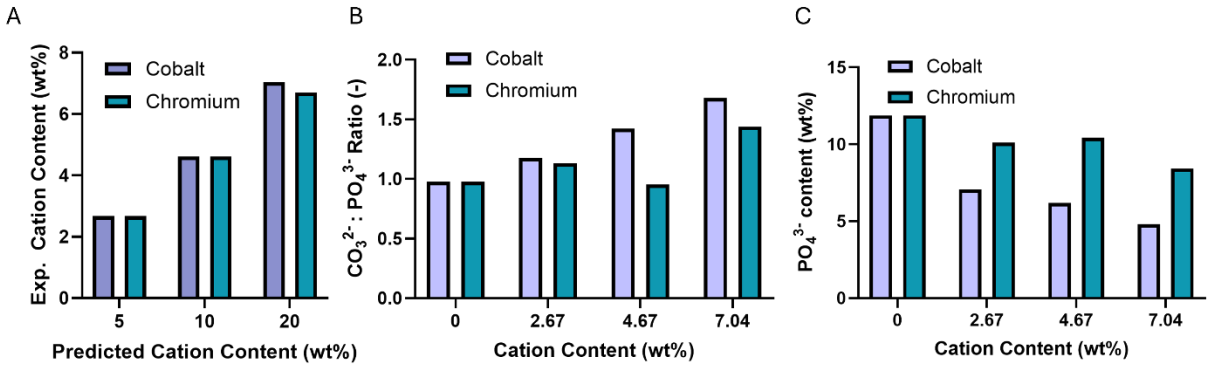


Figure 1: ICP-OES results showing that (A) Approximately half of the predicted cationic concentration (x-axis) was integrated into the crystal lattice. (B) The increase in Co/Cr content was accompanied by an increase in the CHN/ICP-OES determined CO_3^{2-}:PO_4^{3-} ratio in most cases. (C) The total phosphate content is reduced with increasing cation substitution.

2.2 Elemental Analysis

A single vial of each bioapatite sample was sent to Galbraith Laboratories Inc. (Nashville, TN) for elemental analysis. Concentrations of cobalt (Co), chromium (Cr), phosphorous (P), and calcium (Ca) in the bioapatite samples were determined via Inductively Coupled Plasma Optical Emission Spectroscopy (ICP-OES), Fig 1A. Concentrations of carbon (C), Hydrogen (H), and Nitrogen were performed using CHN analysis. Elemental values were converted to carbonate (CO_3^{2-}) and phosphate (PO_4^{3-}) based on molecular weights, Fig 1B,C.

2.3 Lab X-ray Diffraction and Rietveld Refinement

Powder X-ray diffraction (XRD) patterns were collected at room temperature using Bruker D2 Phaser Diffractometer equipped with Cu Kα radiation (λ = 1.5406 Å) operating at 30 kV and 10 mA with an acquisition time of 1.0 s/increment and an increment of 0.02º ranging from 20 to 60° (2θ). XRD spectra for all samples are show in Fig. S2.

Rietveld refinements were performed using BGMN version 4.2.22 with the graphical interface Profex. A carbonated apatite structural model was used as the primary phase for all refinements. Background, scale factor, zero shift, lattice parameters, peak profile parameters, crystallite size/strain parameters (where applicable), and atomic displacement parameters were refined following convergence of the model. Candidate secondary phases were evaluated individually by adding them to the refinement while maintaining the carbonated apatite phase. Phases considered

included calcite, octacalcium phosphate (OCP), α-chromium phosphate (α-$CrPO_4$), guyanaite, cobalt hydroxide, and cobalt bishydrogen phosphate dihydroxide. Refinement quality was assessed using the weighted profile residual (Rwp), expected residual (Rexp), goodness-of-fit (χ^2), and inspection of the observed, calculated, and difference diffraction patterns, Table S3.

2.4 Raman Spectroscopy

Raman spectroscopy was performed exclusively on Co- containing bioapatite samples, as Cr fluoresces under the 785 nm laser, interfering with the signal quality. Spectra were acquired using a Witec α300 Raman spectrometer equipped with a 785 nm laser at a power of ~30 mW. For each sample, ten spectra were collected using a 50X objective lens and an acquisition time of 2 seconds for 45 accumulations per scan. The v_1 phosphate (PO_4^{3-}) peak at 960 cm^{-1} and the v_1 carbonate (CO_3^{2-}) peak at 1070 cm^{-1} were fit as Lorentzian peaks via the Witec Program 5.1 software. Relative carbonate content was estimated by calculating the peak area ratio of the CO_3^{2-} to PO_4^{3-} (1070/960 cm^{-1}) associated peaks, Fig S1B.

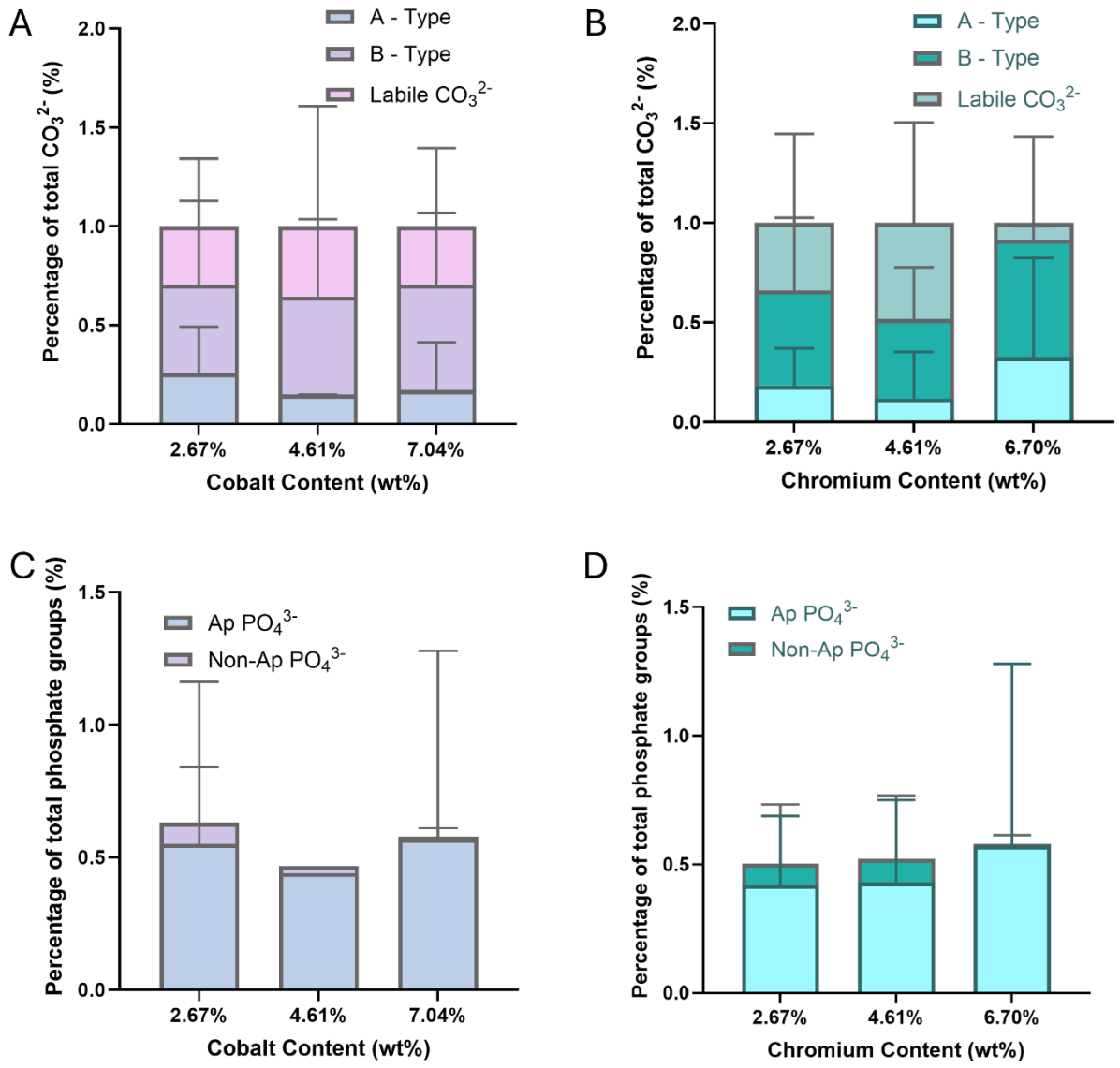


Figure 2: Relative amount of A-type, B-type, and Labile CO_3^{2-} in the (A) Co- containing and (B) Cr-containing bioapatite samples as determined from FT-IR. As well as the relative amount of apatitic and non-apatitic PO_4^{3-} in the (C) Co and (D) Cr-containing apatites. Error bars are the standard error of the peak area fitting.

2.5 Fourier Transform Infrared Spectroscopy (FTIR)

Transmission FTIR was conducted using a Nicolet 5700 spectrometer and OMNIC 8 software (Thermo Nicolet) to further evaluate the structural features and composition of the bone-like apatite phases. Each sample was finely ground, blended with potassium bromide (KBr, Uvasol), and compressed into 7 mm diameter pellets. Two pellet preparations were used: standard absorbance pellets, prepared to yield an absorbance of approximately 1.0 at the maximum v_3 PO_4^{3-} vibration band, and high-absorbance pellets, prepared to yield an absorbance greater than 2.0 at the same band maximum. Standard absorbance spectra were

collected over the 400 to 4000 cm^{-1} range using 64 scans at a resolution of 4 cm^{-1} to observe the v_4 PO_4^{3-}, v_3 CO_3^{2-}, and v_1v_3 PO_4^{3-} vibration modes. High-absorbance spectra were acquired using 64 scans at a higher resolution of 2.0 cm^{-1} to improve the resolution of the v_2 CO_3^{2-}, v_2 PO_4^{3-}, and v_4 PO_4^{3-} vibrational domains. Spectral deconvolution was performed using OriginPro 2021b (OriginLab Corporation, Northampton, MA, USA). For the 400-800 cm^{-1} region, Lorentzian peak fitting was used to identify and quantify the v_2 PO_4^{3-} (~563 cm^{-1}), non-apatitic HPO_4^{2-} (604 cm^{-1}), apatitic HPO_4^{2-} (669 cm^{-1}), apatitic PO_4^{3-} (474, 531, and 542 cm^{-1}), non-apatitic PO_4^{3-} (615 cm^{-1}), apatitic OH^- (579 cm^{-1}), and H_2O (~699 cm^{-1}) contributions. FTIR spectra are shown in Figure S3.

To quantify the carbonate environments, the out-of-plane v_2 CO_3^{2-} deformation region was deconvoluted using initial peak positions corresponding to A-type CO_3^{2-} (~880 cm^{-1}), B-type CO_3^{2-} (~873 cm^{-1}), and labile CO_3^{2-} (~864 cm^{-1}). The B-type CO_3^{2-} contribution was fit using a Lorentzian function, whereas all other bands were fit using Gaussian functions due to their broader peak distributions. The fitted peak areas associated with A-type, B-type, and labile carbonate were normalized to the total carbonate peak area within the v_2 CO_3^{2-} domain. These normalized fractions were subsequently scaled by the total carbonate content of each apatite, determined from the v_3 CO_3^{2-} /v_1v_3 PO_4^{3-} area ratio, to obtain the relative abundance of each carbonate species [23]. These analyses allowed us to confirm the presence of characteristic apatite phases and enabled quantification of the relative abundance of A-type, B-type, and labile carbonate species, as well as the apatitic and non-apatitic phosphate environments (Figure 2).

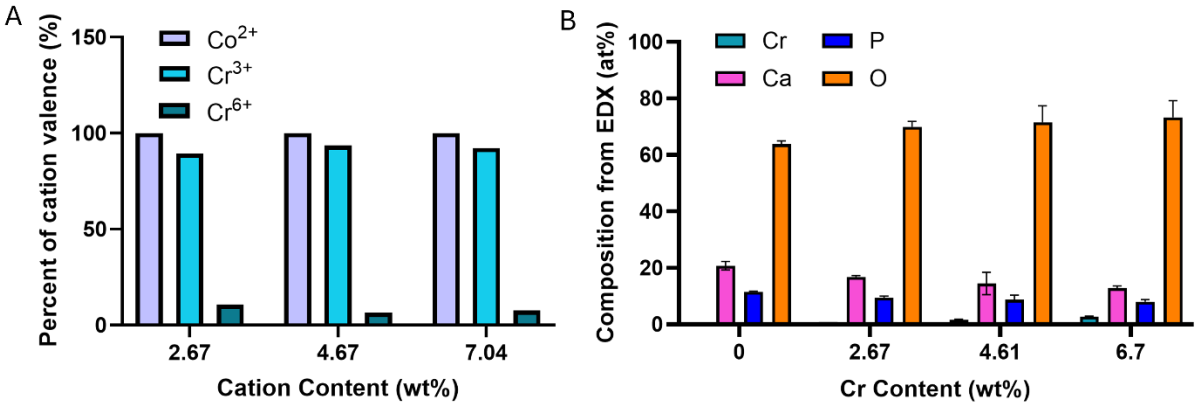


Figure 3: (A) Plot showing the percentages of Co and Cr at each measured valence state. All of the substituted Co has a valence of 2+ while the Cr is primarily Cr^{3+} with some Cr^{6+}. (B) EDX determined atomic composition for the Cr-apatites showing the relative increase in oxygen with increasing Cr. Error bars are standard deviations of the 3 measurements for each sample.

2.6 Valence determination via XPS

Valence of the Co and Cr in the apatites were measured for a single aliquot of each bioapatite sample using X-ray photoelectron spectroscopy (XPS). XPS data were recorded on a

ThermoFischer Scientific spectrometer (Model: K-Alpha, part number: 1200505) with an Al(mono) X-ray source with energy of 1486.6 eV. Sample charging was mitigated using an electron flood gun. X-ray spot size was 400 µm, take off angle was 90°, and analyzer vacuum was at least 5.0 x 10-8 mbar prior to sample processing. Pass energies were 200 and 50 or 25 eV for the survey and core scans respectively. Energy step sizes were 1.0 and 0.1 eV for the survey and core scans respectively. Dwell time was 50 ms. Peak fittings were done using CasaXPS and charge correction was done with reference to the C 1s photoelectron line (284.8 eV).

2.7 Oxygen composition from EDX

Apatite powders were pressed into carbon tape attached to an SEM stub. The apatite was coated with 5nm of Au-Pd to prevent charging. Samples were imaged using a Teneo LV scanning electron microscope (SEM) with a voltage of 20 kV and compositional data was collected using energy dispersive x-ray spectroscopy (EDX). For each sample, 3 areas were selected and EDX was run for a live time of 164 sec. Percentages of Oxygen, Phosphorus, Calcium, and Chromium were measured for each sample using the instrument software, Fig 3.

2.8 Computational Modeling Using Density Functional Theory

The apatite crystal is modelled as an orthorhombic cell for DFT calculations, in which the crystal's hexagonal primitive cell with 44 atoms [24-29] (space group P63/m and a 50% partial occupancy of the OH sites) is doubled along its *b*-axis to maintain lattice periodicity. Hydroxyapatite unit cells include tightly bonded PO_4^{3-} tetrahedral units, Ca ions in two potential sites, and OH groups oriented along the crystalline *c*-axis. From the hydroxyapatite unit cell, we then generate computational models of apatites with carbonate substitution and substitutional concentrations of 3, 5 and 8 wt% Cr and 3, 6, and 9 wt% of Co, Table S2. We developed apatite unit cells with CO_3^{2-} wt% similar to the experimental samples such that their corresponding ratio of A:B-type carbonate substitution is same. Carbonate concentration is approximately constant in all Co apatite crystals (8.8-9wt%) and Cr apatite crystals (11.8-12.2wt%). These concentrations capture the carbonate content difference between the experimental Co and Cr apatite samples. However, labile carbonate substitution is excluded due to lack of surface in the periodic unit cell. For the apatites with Co substitution, the Ca^{2+} are substituted with the Co^{2+} cation. During preliminary study, we determined that carbonated apatites with Co substitution at Ca(1) or Ca(2) sites have minimal ground state energy difference between them. Furthermore, we compare apatites with a higher concentration of Co substituting only Ca(1) sites and mixed Ca(1) and Ca(2) sites and find an energy difference less than the ionic minimization energy convergence threshold (~1.4meV) of the DFT calculations. Thus, it is likely that Co substitution occurs in both Ca sites in the experimental apatite samples, which has also been reported previously [30]. The Cr substitution is performed by substituting Cr^{3+} for Ca^{2+} in the Ca(2) site near OH^- channels based on parametric studies, experimental findings, and

previous studies [31-34]. During our preliminary study, we predict Cr^{3+} substitution of Ca(2) sites is ~1.3eV more favorable (lower) than Ca(1) sites. We exclude Cr^{6+} substitutions, which appear in the experimental apatite samples, due to very low concentration. Interstitial oxygen (O_i) is added with a 1:1 ratio for Cr:O based on the experimental finding that O wt% increases with increasing Cr wt%, Fig. 3B. O_i is suggested by Lima et al., [33] as a charge compensation mechanism for Cr^{3+} substitution of Ca^{2+} in carbonated apatite. Computational models of the apatites are shown in Figure 5E, and all apatites are modelled using the visualization software OVITO [35] and VESTA [36].

To predict the lattice and elastic constants of the apatite crystals, we use Quantum ESPRESSO [37, 38] with ultrasoft pseudopotentials [39-41] and PBE exchange-correlation functional type [42]. We also use a kinetic energy cutoff of 1225 eV (90 Ry) and a *2x2x2 K*-point mesh based on energy convergence studies, which are included in the supplemental materials as Table S4 and Figure S7. To correct for dispersion forces, we use Grimme's DFT-D2 van der Waals scheme [43-45]. An energy convergence threshold of 1.36 x 10^{-5}eV (10^{-6}Ry) is used based on parametric studies to reach ground state energy. We perform a variable-cell relax calculation to find the lattice constants of the apatites, followed by relaxation calculations for elastic constant predictions.

We find the elastic constants of a material to measure its stiffness and resistance to deformation, and DFT has been shown to be a useful resource for predicting these values [24, 25]. In previous studies, DFT predictions for hydroxyapatite crystals have been validated experimentally [18, 26]. Hydroxyapatite crystals with substitutions have also been successfully modelled using *ab initio* methods for both A- and B-type carbonate substitutions, as well as K and Na cationic substitutions [45-48]. These validations, in addition to DFT's ability to predict the mechanical properties of crystals with Co or Cr with ultrasoft pseudopotentials and PBE functional type [49, 50], support our use of DFT to study apatites substituted with Co and Cr. The elastic constants are computed by fitting Hooke's law for energy-strain relations for infinitesimal deformation [51]. We apply a minimum of six strains $\varepsilon_{\alpha\beta}$, $\alpha, \beta \in (a, b, c)$ within a range of -1% to 1.5% to the apatite crystals substituted with Co and Cr to obtain the C11, C33, C12, and C13 elastic constants. The ground state energy versus lattice strain is plotted to obtain elastic constants corresponding to each direction (*a*, *b* and *c*), as described in our previous work [18]. The bulk modulus for each concentration of Co and Cr apatites are predicted as described in section 2.9.

2.9 Mechanical Testing

Mechanical testing was performed on two aliquots from each bioapatite batch. Apatite crystal powders were packed into the 7 mm^3 cavity of sample holders with two flexible X-ray transparent

polyimide (Kapton) windows. 100% ethanol (EtOH) was then added to the cavity to ensure the powders were suspended in fluid and the sample carrier was sealed with an O-ring screw. The sample holders were then placed in a custom-made pressurization chamber with X-ray transparent entry and exit diamond windows encasing the sample [19, 48, 52-54]. Tap water was then utilized in this chamber as a pressurizing fluid, which never interacted with the powder sample. Water and ethanol are slightly compressible (K = 2.15 and 0.9 GPa, respectively); however, they remain an excellent means to apply pressure to the apatite nanoparticles. The fluids were manually pressurized via a screw pump such that the powders were gradually compressed in increments of ~100 MPa up to ~500 MPa and were returned to the starting pressure of ~100 MPa to ensure reversibility of the detected changes. The applied pressure range exceeds physiological stresses typically experienced by bone tissue. However, these elevated pressures were intentionally employed to generate measurable changes in apatite lattice parameters and enable comparison of the pressure-dependent mechanical response of the substituted apatites. Similar high-pressure diffraction approaches have been widely used to investigate the elastic compressibility and structural stability of apatite and other mineralized materials [52, 53]. Furthermore, the stress-strain relationships remained linear over the applied loading range (Fig. S4), indicating that the materials remained within the elastic deformation regime and that no evidence of nonlinear or irreversible deformation was observed.

The pressure chamber was mounted at the P07 High Energy Materials Science beamline at the Petra III synchrotron radiation source (DESY, Hamburg, DE) in the experimental hutch EH3. The pressure chamber was oriented such that the 1 x 1 mm^2 73.3 kV X-ray diffraction beam passed through the diamond and Kapton windows, interacting with the pressurized bioapatite samples and thereafter exiting toward the detector. The lanthanum hexaboride (LaB6) calibrated sample to detector distance, z, was 2.54 m and was selected to guarantee that both the apatite (002) and (310) peaks were recorded. Two diffraction patterns were captured at each load increment on a 2048 x 2048-pixel Si detector (Perkin Elmer) with an acquisition time of 10 seconds. Sample holders containing only ethanol were also run at each load to obtain background diffraction images.

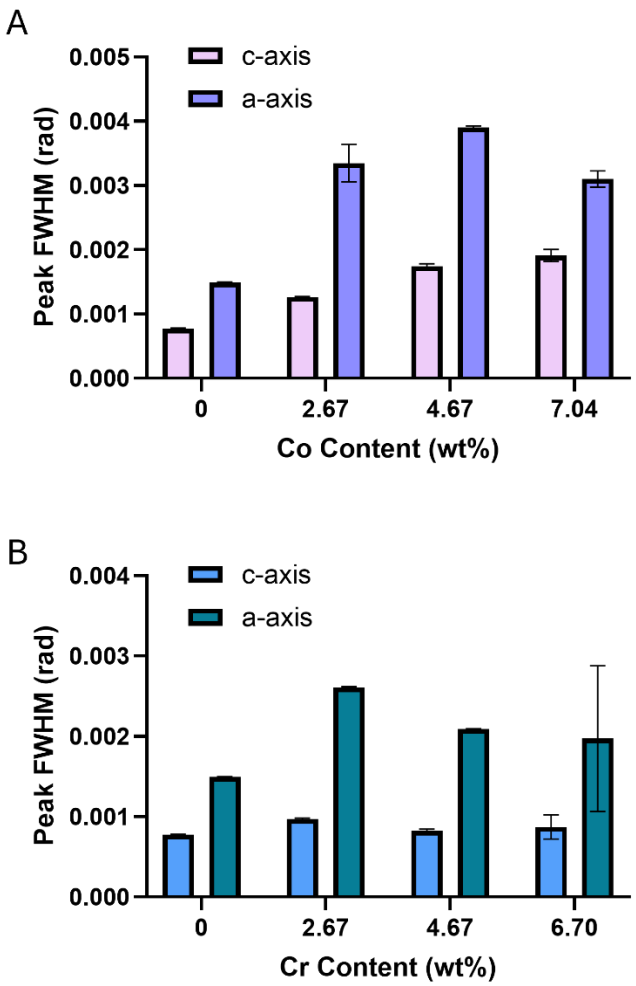


Figure 4: Full width at half maximum (FWHM) of the c-axis (002) and a-axis (310) peaks for (A) Co- and (B) Cr-containing bioapatites as determined from WAXS. Error bars are the standard deviation of the 2 measurements for each bioapatite sample.

Background patterns taken for the ethanol at each load were subtracted from the bioapatite powder spectra. The apatite (002) and (310) peaks were fit using a pseudo- Voight function to find the average peak center (R) and full width at half maximum (FWHM, Fig 4) for each angular position (φ). Because of hydrostatic stress as well as the random dispersion of the powder, R and FWHM remained constant across all φ; consequently, average of R(φ) and FWHM(φ) were used for all diffraction patterns, Fig 4. The peak center, R_{ave}, was then converted to d-spacing according to the equation: $d = \lambda/2\sin(R/z)$, assuming a small diffraction angle, Figure 5A-D. The d-spacings were converted to lattice spacing assuming a hexagonal unit cell. The lattice strain was calculated using the equation $\varepsilon = (d_o - d)/d_o$. The (002) peak strains, representing deformation along the crystal c-axis, are referred to as ε_{33}. The (310) peak strains, representing deformation along the a-axis, are referred to as ε_{11}. The strains can be plotted as a function of applied stress to determine the linearity of the deformation, Fig S4. The strains are used to determine the change in unit cell volume, ΔV/V. The slope of ΔV/V as a function of applied stress is the bulk modulus of the apatite, K, Fig 6.

2.10 Determination of the Compliance Tensor

In hydrostatic loading, there is no shear loading and as a result, the stress (σ) and strain (ε) tensors exhibit the following diagonal form in Cartesian coordinates:

$$\sigma_{jk} = \begin{bmatrix} \sigma_{11} = \sigma & 0 & 0 \\ 0 & \sigma_{22} = \sigma & 0 \\ 0 & 0 & \sigma_{33} = \sigma \end{bmatrix} \quad (1)$$

$$\varepsilon_{jk} = \begin{bmatrix} \varepsilon_{11} & 0 & 0 \\ 0 & \varepsilon_{22} & 0 \\ 0 & 0 & \varepsilon_{33} \end{bmatrix} \quad (2)$$

Since hydroxyapatite exhibits hexagonal symmetry, it is known that $\varepsilon_{11}=\varepsilon_{22}$ and that the compliance tensor can be completely determined with only five independent constants: C_{11}, C_{12}, C_{13}, C_{33}, and C_{44} [55, 56]. These five independent elastic constants are computed using DFT as described in the methods section. The measured strain results can be related to the compliance tensor by calculating: η and K. The ratio $\eta = {}^{\varepsilon_{11}}/_{\varepsilon_{33}}$ is related to the compliance tensor according to:

$$\eta = \frac{\varepsilon_{11}}{\varepsilon_{33}} = \frac{C_{33}-C_{13}}{C_{12}+C_{11}-2C_{13}} \quad (3)$$

K, the bulk modulus, is a measure of how resistant the material is to compression. It is related to the measured strain and the elastic constants according to the following equation:

$$K = \frac{\sigma}{{}^{\Delta V}/_{V}} = \frac{\sigma}{2\varepsilon_{11}+\varepsilon_{33}} = \frac{[(C_{11}+C_{12})C_{33}]-2C_{13}^2}{C_{11}+C_{12}+2C_{33}-4C_{13}} \quad (4)$$

This leaves us with two measurable physical parameters, η and K, and 4 independent variables: C_{11}, C_{12}, C_{13}, and C_{33}. Using established optimization techniques and setting bounds based on DFT calculations we can develop accurate guesses as to the compliance tensor of these different apatites.

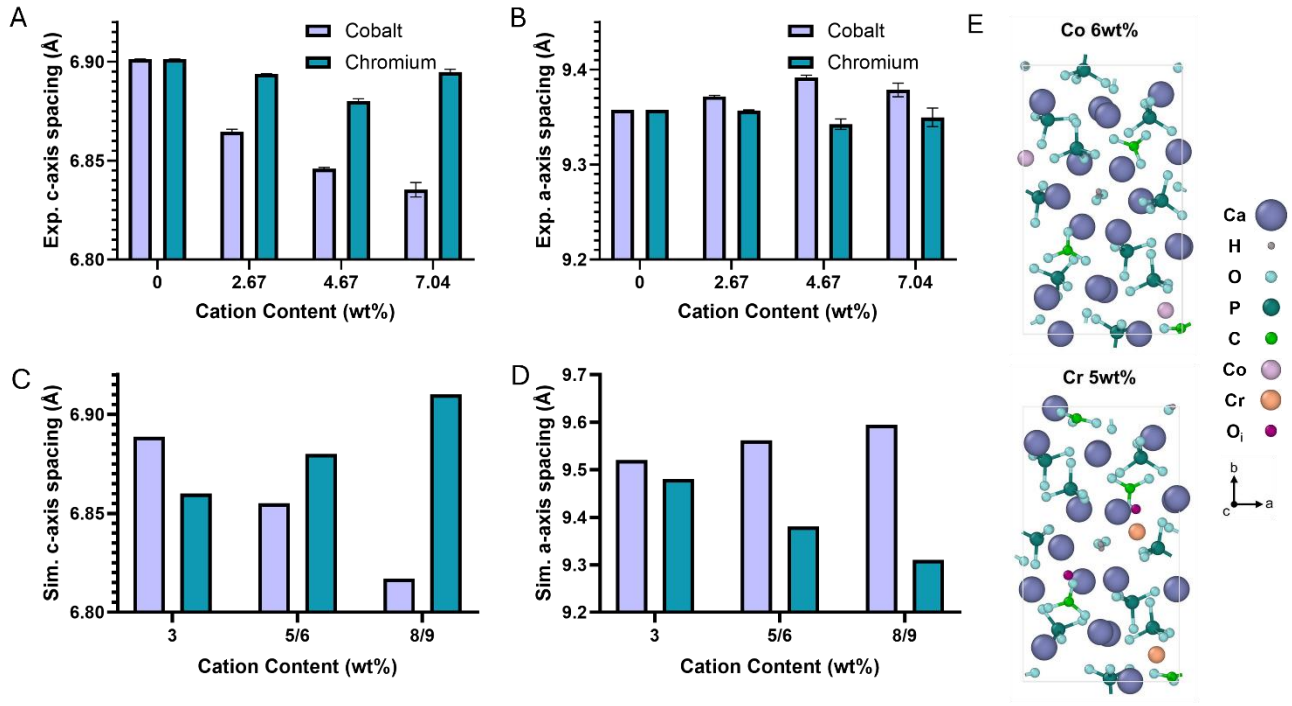


Figure 5: Experimental (A&B) and simulated (C&D) lattice spacings along the c-axis (A&C) and a-axis (B&D) for Co and

Cr containing apatites with (E) DFT models of the apatites. Experimental error bars are the standard deviation of the two XRD measurements.

2.11 Optimization

To optimize the values of C_{11} , C_{12} , C_{13} , and C_{33} from the hydrostatic data, two assumptions were made: (1) the optimized values must result in K and η equal to the experimental values and (2) the residual sum of square differences between the optimized values and DFT-determined initial guesses must be minimized [19, 52] . Initial guesses of C_{11}, C_{12}, C_{13}, and C_{33} were taken from the DFT computational models described above. Guess variability in the form of a standard deviation from the mean compliance values was added to the optimization to account for possible discrepancies between then guesses and experimental values. These were run with standard deviations of 1, 5, and 10 GPa to confirm that the results converged to the similar values and that the optimization was sensitive and accurate. Using the mean calculated C_{11}, C_{12}, C_{13}, and C_{33} and a standard deviation of 1 GPa at each composition from the DFT computational model predictions, the elastic constants were linearly interpolated between 0 and 8/9 wt% cationic substitution. At each value of concentration, the elastic constants were randomly generated from a normal distribution with the mean parameter being calculated from the mean and standard deviation values determined from DFT. With established guesses, the elastic constants were optimized using the previously discussed assumptions. Since elastic constants were optimized for each of the 6 measured stresses for each sample, sample internal variability was accounted for in addition to guess variability. The optimized values of C_{11} , C_{12} , C_{13} , and C_{33} were then used to calculate the compliance of the samples according to the equations [52]:

$$S_{11} = \frac{C_{33}C_{11} - C_{13}^2}{[C_{33}(C_{11}+C_{12}) - 2C_{13}^2](C_{11}-C_{12})} \quad (5)$$

$$S_{33} = \frac{C_{11}+C_{12}}{C_{33}(C_{11}+C_{12}) - 2C_{13}^2} \quad (6)$$

The Young's moduli of the crystals can then be determined from these values using [55, 57]:

$$E_{11} = E_{22} = \frac{1}{S_{11}} \quad (7)$$

$$E_{33} = \frac{1}{S_{33}} \quad (8)$$

A Monte Carlo simulation was run 10,000 times across the Co/Cr concentrations to account for variations in the compliance tensor optimization and the mean E_{11} and E_{33} are reported, Fig 7.

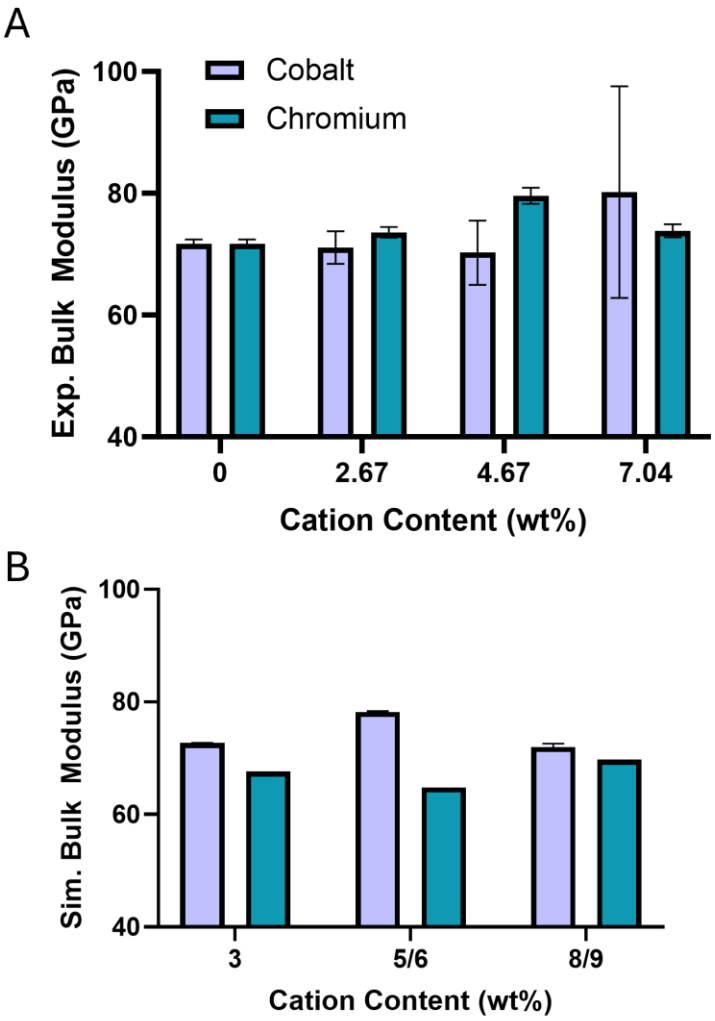


Figure 6: Experimental (A) and simulated (B) Bulk Moduli for the Co- and Cr-containing apatites. Experimental error bars are the standard deviation of the bulk moduli from 2 XRD measurements for each bioapatite sample.

3 Results

3.1 Bioapatite Synthesis

Using the direct precipitation method, Co and Cr-substituted bioapatite samples were successfully synthesized. The Co- substituted samples exhibited a lavender hue, which deepened with increasing cobalt concentration, while Cr-substituted samples appeared jade green, also showing progressively darker coloration at higher concentrations. The WAXS, Raman (Co-containing apatites only), and FTIR analyses of the Co- or Cr-containing powders confirm the apatitic characteristics of the synthesized biomimetic apatites.

3.2 Co and Cr Cations were successfully incorporated into apatites

The direct precipitation method resulted in approximately half of the calculated ion concentration being incorporated into the hydroxyapatite lattice. As shown in Figure 1A, the theoretical ion concentrations are based on initial solution compositions for both Co and Cr were calculated to be 5%, 10%, and 20%. However, only 2.67% of the 5%, 4.61% of the 10%, and 7.04% of the 20% were substituted in the Co-containing apatite samples. The Cr-containing samples followed a similar trend, although the 20% sample only incorporated 6.70%.

Rietveld refinement was performed for the 5, 10, and 20 wt% Cr- and Co-substituted apatite compositions using a carbonated apatite structural model. Good agreement between the calculated and experimental diffraction patterns was obtained for all samples (Rwp = 1.45–4.59%, χ^2 = 1.0–1.4). Candidate secondary phases, including calcite, α-$CrPO_4$, guyanaite,

cobalt hydroxide, cobalt bishydrogen phosphate dihydroxide, and octacalcium phosphate (OCP), were also evaluated. Chromium- and cobalt-containing secondary phases refined to zero or negligible phase fractions. Complete refinement statistics and phase fractions are provided in Table S3.

The Co samples exhibited a valence of 2+ in all cases, Fig 3A. The Cr in the Cr-containing apatites substituted as either Cr^{3+} or Cr^{6+}. Most of the Cr, 92±2%, was present as Cr^{3+} with Cr^{6+} representing less than 10% of the total substituted chromium. The ratio of Cr^{6+}/Cr^{3+} did not vary significantly between samples.

3.3 Carbonate-to-Phosphate ratio is affected by cationic substitutions

The weight percent of carbonate in the apatites was relatively constant irrespective of cation substitution concentration. The Co-containing apatites had an average CO_3^{2-} wt% of 8.4±0.4 while the Cr-containing apatites had a an average wt% of 11.2±1.1. To match these results, the wt% CO_3^{2-} in the DFT models was set to 8% and 12% for the Co- and Cr-apatites, respectively.

The carbonate to phosphate ratio (CO_3^{2-}:PO_4^{3-}), used to quantify the relative carbonate content within the apatite, was evaluated using Raman spectroscopy (Co-containing apatites only), FT-IR, and CHN/ICP-OES, Fig 1B,C and S1. Elementally, the CO_3^{2-} levels were determined form the CHN-measured carbon, and the PO_4^{3-} concentrations from the ICP-OES-measured phosphorous. As can be seen in Figure 1B, the relative CO_3^{2-} content increased with increasing Co-substitutions. Since the CO_3^{2-} concentration remains relatively constant, this indicates that there is a drop in PO_4^{3-} content with increasing Co concentration. This trend is less apparent in the Cr-containing samples with the 4.61 wt% Cr-apatite exhibiting the lowest of CO_3^{2-}:PO_4^{3-} ratio.

The Raman (Co-containing apatites only) and FTIR relative carbonate content is determined from the area ratio of the CO_3^{2-} peak area to that of the PO_4^{3-} peak. This CO_3^{2-}:PO_4^{3-} ratio agrees with the ICP-OES/CHN results showing an increase in CO_3^{2-}:PO_4^{3-} with Co and Cr substitution with the exception of the 4.61% Cr-containing apatite, Figure S1.

FTIR analysis of the CO_3^{2-} location in the Co- and Cr-substituted apatites using the v_2 CO_3^{2-} peak showed that the mineral predominately exhibits B-type carbonate substitutions (CO_3^{2-} replacing PO_4^{3-} groups), Figure 2A&B. The CO_3^{2-} location does not seem to be affected by Co or Cr substitutions. FTIR was also used to determine the distribution of phosphate groups using the PO_4^{3-} peaks around 600 cm^{-1}, Figure 2C&D. The total amount of apatitic phosphate was reduced in the Cr samples compared to the Co apatites, but it did not change significantly with wt% of substitutions. However, the amount

of non-apatitic PO_4^{3-} decreased with increasing Co and Cr content.

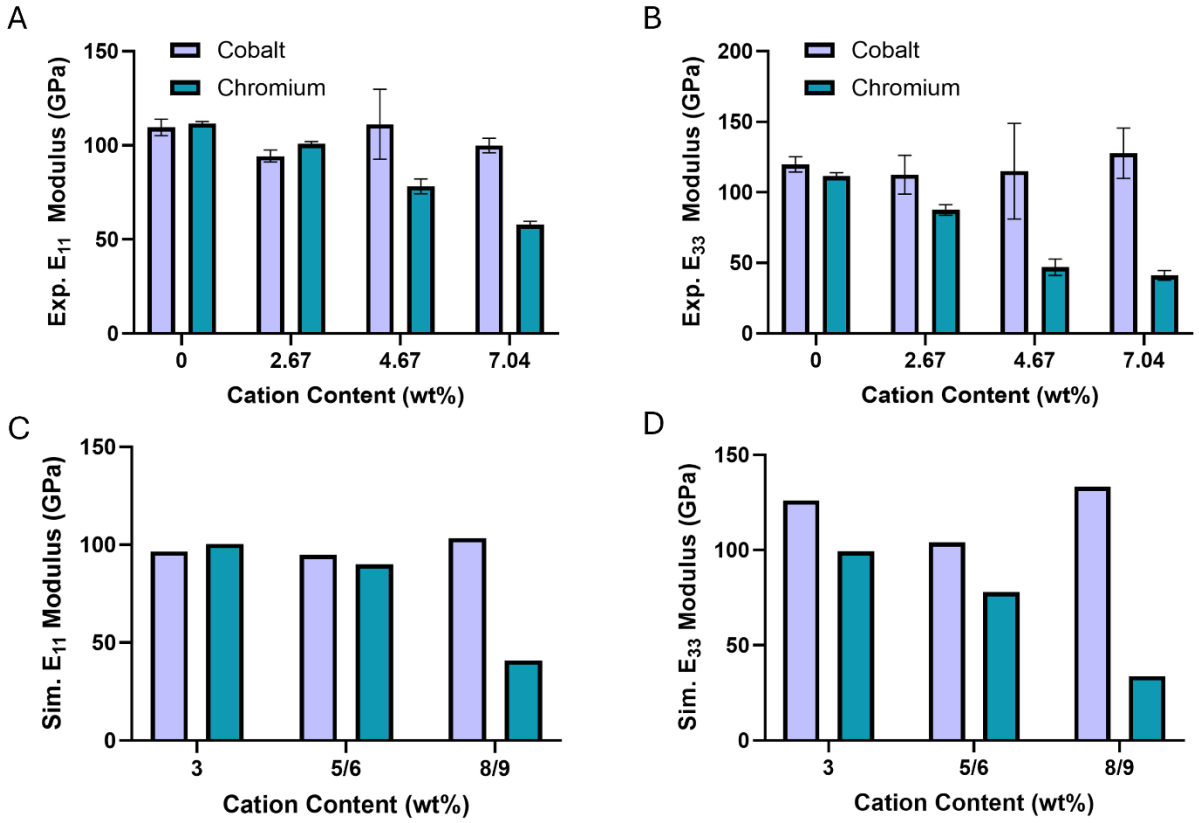


Figure 7: Experimental (A&B) and simulated (C&D) Young's moduli for the Co- and Cr-containing apatites along the a- (A&C) and c- (B&D) axis. Error bars represent the standard deviation of the 10,000 Monte Carlo simulations used in the compliance tensor optimization.

3.4 Cationic substitutions affect crystallinity but minimally affect lattice spacing

The crystal full width at half maximum (FWHM), an indicator inversely related to crystallinity, was plotted for all concentrations of Co and Cr, Fig. 4. In Co-containing samples, increasing concentrations of Co ions increased the FWHM and therefore reduced the crystallinity along the c-axis (002) while the a-axis (310) planes exhibited an initial increase followed by a drop in FWHM at 7.04% Co. For the Cr-containing samples, the FWHM of both the c- and a-axes showed a decrease in FWHM with increased Cr concentration after 2.67%.

The crystal lattice spacings along the c-axis (002) and a-axis (310) were analyzed for all concentrations for both Co and Cr, Fig. 5. Incorporation of Co into the apatite increased the a-axis lattice spacing while decreasing the c-axis lattice spacing. The inclusion of Cr ions resulted in an initial decrease in the c-axis lattice spacing followed by an increase at 6.7% Cr while the a-axis remained relatively unchanged.

The computational models developed using the compositional data described in sections 3.2 and 3.3 were employed to predict the experimental lattice spacing values. Trends

in lattice spacing as a function of Co content were well matched in both the a- and c-axis although the experimental a-axis values were consistently smaller than the computational model predictions. For the Cr apatites, we predict similar lattice spacing trends at higher wt% of Cr substitution. The experimental and computational c-axis spacing trend is overlapping >4%, though the DFT prediction at 3wt% Cr is less than experimental at 2.67wt% Cr. However, the maximum lattice spacing difference between methods for the 2.67-3wt% Cr apatite is minimal; there is only 0.4% difference of the c-axis and 1.4% of the a-axis. Quantitative differences between experimental and computational lattice spacings are shown in Table S6. Lattice parameter variances may be due to presence of labile carbonate on the surface of the experimental apatite samples which represents ~30% of the CO_3^{2-} content (Fig 2) in most samples and is not included in the computational modeling of the unit cell. The computational apatite models are used to predict the bulk properties of apatites, but the surface effects are not included in the fully periodic DFT calculations. Thus, the contribution of labile carbonate to the structural and mechanical properties observed in experimental apatite samples is not fully captured in the computational models. The maximum a-axis spacing difference between the experimental and computational apatites is ~2.2% with ~7-9wt% Co substitution. The maximum c-axis spacing difference is ~0.4% for the apatites with ~3wt% Co and ~3wt% Cr. Labile carbonate exclusion in the computational models may be a source of these minor differences between the experimental and DFT findings. When comparing the computational and experimental data of the lattice properties of Cr apatites, the low Cr^{6+} substitution content likely also causes a small difference between both results.

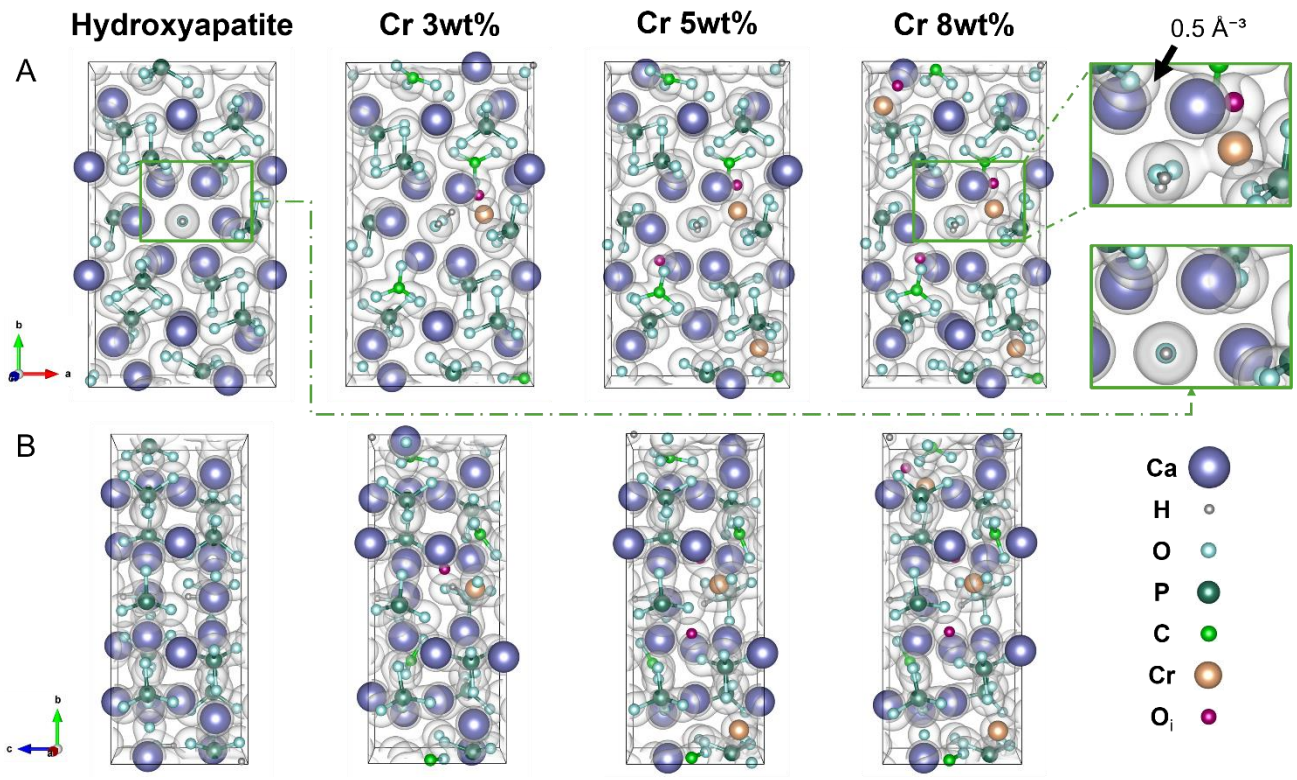


Figure 8: Isosurface of electron density greater than 0.5 Å $^{-3}$ for hydroxyapatite and Cr apatites with visualization in the A) a-axis and B) c-axis

3.5 Mechanical Properties via WAXS Stress-Strain & Bulk Modulus:

The WAXS determined lattice strain was plotted as a function of the applied hydrostatic stress. These stress-strain diagrams appear linear, indicating that all loading remained in the elastic zone, Fig S4. The bulk modulus of the crystals was determined from the slope of the volumetric change in the crystal lattice, as calculated from ε_{11} and ε_{33}, plotted as a function of the applied stress. The Bulk moduli exhibited very little change as a function of cationic content in both the Co- and Cr-apatites, Fig 6. The values are similar to those predicted by DFT.

The elastic constants were optimized as described in Section 2.10 for each Co and Cr composition. For the Co apatites, the elastic constants appear to rise up to a cationic concentration of approximately 5wt% after which they substantially decreased, Fig S5. Although the values are similar between the simulated and experimental elastic constants, there are discrepancies especially around 5wt% cationic substitutions. The elastic constants of the apatites with Cr show more variance with increasing Cr wt%. The uniaxial elastic constants (C_{11} and C_{33}) decrease for the apatites with high Cr wt%. This decrease is mostly linear with respect to the Cr wt% for C_{11} and C_{33} predicted with DFT and C_{33} found experimentally. However, experimental C_{11} increases slightly up to 4.61wt% before dropping significantly for 6.7wt% Cr. The simulation and experimental C_{12} and C_{13} of the Cr apatites match well for high Cr wt%, though there is some discrepancy for the apatites with ~5wt% Cr. For the 4.61-5wt%

Cr, the elastic constant differences are up to ~30 GPa between DFT and experimental methods. This may be due to high percentage of labile carbonate (48% of the total carbonate, Fig 2B) in the 4.61 wt% Cr apatite, which we have noted as a potential cause of variance between experimental and DFT findings.

Using the optimized compliance values, the Young's modulus of the crystals along the a- and c-axes were calculated. They do not show a clear trend with Co cation substitution, although their numerical values are similar to those seen in the DFT models, Fig 7. With increasing Cr wt%, DFT and experimental methods both predict notable decrease of Young's modulus along the a- and c-axes. At the highest studied Cr wt%, the Young's moduli are nearly halved along both axes. Differences in the experimental and computational E_{11} and E_{33} values are shown in table S7.

4 Discussion

The substitution of Co and Cr ions into the apatite lattice has profound implications for the structural and mechanical properties of bioapatite, especially considering their use in MoM hip implants. The incorporation of these ions into bone minerals can influence the stability, stiffness, and brittleness of the mineral, which may impact both the function and longevity of these implants. This discussion examines the observed changes in the bioapatite structure, the mechanical properties of the synthesized materials, and the ion-specific effects of Co and Cr, independently. Understanding these effects is critical for predicting how such substitutions might behave in vivo and their potential influence on bone health and implant outcomes.

The Co- and Cr-substituted bioapatite samples were successfully synthesized via the direct precipitation method. However, the substitution efficiency of both the metals was lower than predicted with approximately 50% incorporation, Fig 1A. It is possible that the ionic radii of cobalt and chromium (70 pm and 87 pm, respectively), which differ from calcium (99 pm)[48-50]; hinder their efficient substitution into the lattice structure. The relatively low substitution efficiency may also result from competitive ion incorporation, as the synthesis process involves multiple ions vying for positions in the lattice.

All of the cobalt present in the Co-containing apatites substituted as Co^{2+} in agreement with previous studies [58, 59], Fig 3. Co substitutes for Ca^{2+} at either the Ca(1) or Ca(2) site with no need for further charge balances [59]. Chromium on the other hand has a more complex substitution pattern. The valence of Cr in apatite has been reported as being 6+, 5+, or 3+ [33, 60-64]. In the 6+ and 5+ cases, the chromium forms chromate (CrO_4^{2-}) which then substitutes for the phosphate ions in the lattice structure [60, 61]. Conversely, in the 3+ case, the Cr substitutes for calcium in either site; however, in order to maintain charge balance, it is

associated with oxygen vacancies or interstitial oxygen [33, 62, 64]. XPS results indicate that the Cr-containing apatites primarily exhibit Cr^{3+} with less than 10% of Cr^{6+}, Fig 3A. To confirm whether charge balance was regulated via oxygen vacancies or addition of interstitial vacancies, EDX was performed on the Cr-containing samples to determine the relationship between Cr and oxygen. EDX results indicate that oxygen increases with increasing Cr content, Fig 3B, suggesting that the presence of interstitial oxygen is most likely correct as suggested by [33]. As previously mentioned, all of the DFT models for the Cr apatites use interstitial oxygen.

Raman (Co-containing apatites only), FTIR, and ICP-OES/CHN revealed that despite the relatively constant CO_3^{2-} concentration in the apatites, the increasing concentrations of Co and Cr ions resulted in a loss of PO_4^{3-}. The cationic concentration was extremely well correlated to the phosphate content (CI: -0.95 and -0.93 for Co and Cr, respectively, Table S5). This is in agreement with the literature in which increased Cr content was associated with phosphate deficiency [64]. In Na^+ and K^+ substituted biomimetic apatites, changes to the PO_4^{3-} alongside the substitution of the monatomic cations is attributed to the necessary charge balance needed when Na^+/K^+ substitutes for Ca^{2+} [16, 19, 21]. However, in this case, the Co has a valence of 2+ and Cr^{3+} is charge balanced by oxygen suggesting that charge balance is not the driving force. There could be steric motivations caused by the substitution of trigonal CO_3^{2-} molecule for the tetrahedral PO_4^{3-} ; however, the lack of change in the location of the CO_3^{2-} substitutions eliminates the possibility that a shift in the CO_3^{2-} locations is responsible for the loss of PO_4^{3-}. McConnell suggested that PO_4^{3-} maybe replaced by H_4O_4 in hydrated systems, but no consistent changes in mineral hydration were measured [65]. Our FTIR results indicate that the loss of PO_4^{3-} seems to occur primarily within the non-apatitic PO_4^{3-} located within the surface hydrated layer and not within the apatitic core. The labile CO_3^{2-} in the hydrated layer does not change with Co or Cr suggesting that these heavy metals are having a specific effect on the surface phosphates and not in eliminating the hydrated layer in general.

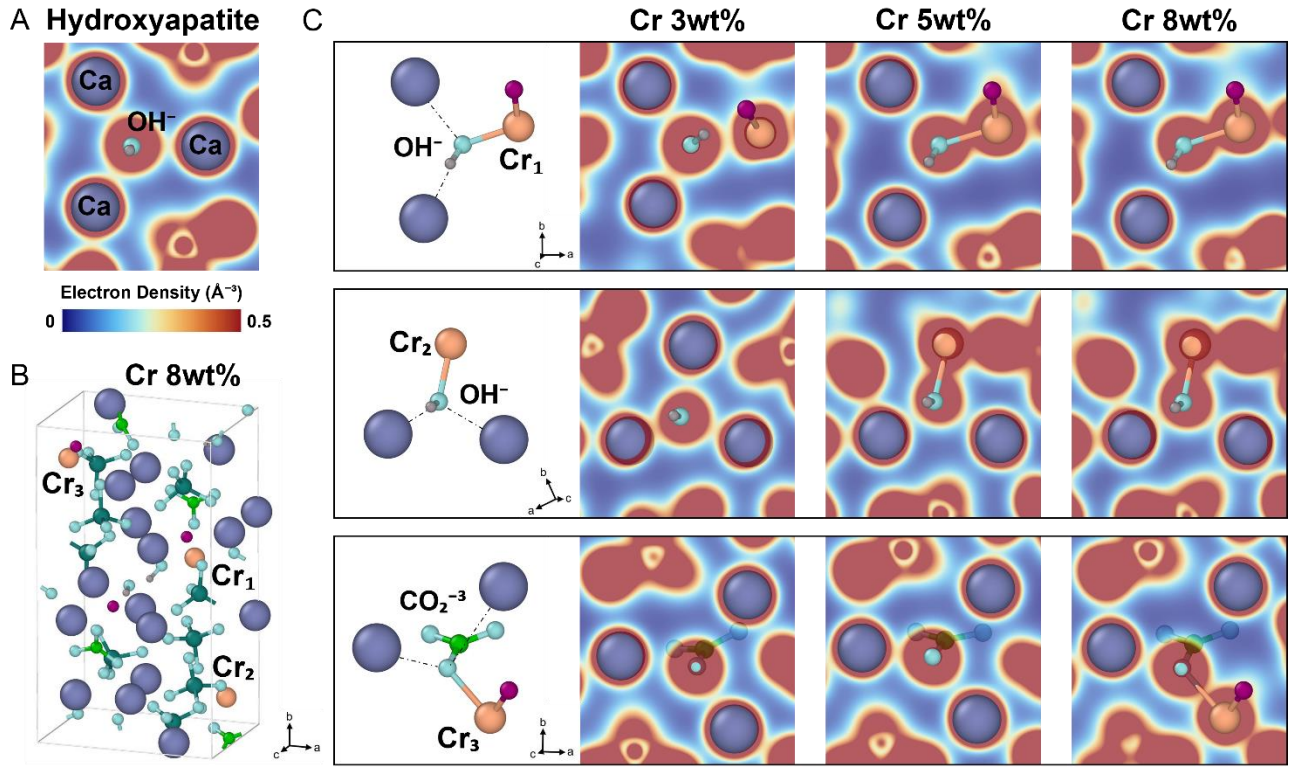
The preferential reduction in non-apatitic phosphate without a corresponding decrease in labile carbonate suggests that Co and Cr do not simply eliminate the hydrated surface layer of the apatite crystals or increase their maturation. Instead, these findings indicate that the heavy metal ions selectively modify the phosphate chemistry within this hydrated layer. One possible explanation is that Co and Cr alter apatite crystal growth and maturation, resulting in reduced incorporation or retention of phosphate in non-apatitic environments while leaving the carbonate-rich surface layer largely intact. Previous studies have similarly demonstrated that Co^{2+} and Cr^{3+} modify hydroxyapatite crystal growth, producing changes in crystallite size, crystallinity, and lattice parameters [66]. Although the present data do not distinguish whether

these effects arise from altered nucleation, crystal growth kinetics, or local metal-phosphate interactions, the collective evidence suggests that Co and Cr influence the evolution of the hydrated surface layer during apatite formation rather than simply adsorbing to the crystal surface.

Generally, the addition of substitutions to apatite crystals results in deformation of the lattice and a decrease in the mineral crystallinity [16, 18, 21]. However, these behaviors were not obvious in the Co and Cr substituted samples. Although the crystallinity of Co-containing apatites generally decreased with increasing Co-content, there was a recovery in the a-axis at high Co concentrations. Substitution of Co into apatite is associated with decreases in both the c- and a-axis lattice spacing [59]. Increasing CO_3^{2-}:PO_4^{3-} ratios are associated with an increase in the c-axis and a decrease in the a-axis lattice spacing [16, 18, 67, 68]. However, the Co-apatites here exhibit a decrease in the c-axis and an increase in the a-axis suggesting that the addition of the Co is countering the lattice deformations associated with CO_3^{2-} and PO_4^{3-} , this despite the fact that Co is only slightly smaller than the Ca for which it substitutes. The discrepancy in the a-axis compared to [59] may be due to differences in the location of the Co ion between the Ca(2) and Ca(1) site. This is supported by the agreement between experimental and DFT lattice parameter predictions of the apatites. We attribute the minimal lattice parameter variances between the computational model prediction and experimental values to a lack of inclusion of labile carbonate and phosphate variations in the DFT models. The labile carbonate is present on the surface of the apatite and makes up nearly 30% or more of total carbonate content in most apatites in this study (excluding the apatite with 6.7wt% Cr). However, the computational model utilizes a periodic unit cell with no free surfaces and

therefore cannot account for this surface contribution.

Figure 9: (*A) Electron density in OH⁻ channel of hydroxyapatite, (B) DFT model of apatite with 8wt% Cr and C) the*



electron density of the OH⁻ channels corresponding to the Cr notated in panel B in all Cr apatites

Even more poignant, the Cr-containing apatites exhibited an increase in the mineral crystallinity with increasing Cr. This points to the regular and cohesive incorporation of substitutions in such a way that the crystal lattice is minimally disturbed. Further, lattice spacing for the Cr-containing apatites remains relatively unchanged despite the changes in composition. Once again indicating that the interactions between Cr, PO_4^{3-} and CO_3^{2-} are working to minimize internal stresses. It is possible that although CO_3^{2-} substitutions and PO_4^{3-} loss alter the local atomic structure of the lattice, the resulting distortions may not significantly disrupt the overall organization or compromise the mineral's macroscopic integrity [69]. This could be due to changes primarily affecting the hydrated surface layer, or due to compensatory mechanisms within the lattice, such as subtle shifts in crystal orientation in the presence of Co and Cr substitutions. For example, other cations such as Na^+ and K^+ can significantly alter the lattice and directly influence the location of carbonate CO_3^{2-} ions [21]. Na tends to substitute at Ca(2) sites, which promotes favored B-type carbonate substitutions, while K shows concentration-dependent shifts between Ca(1) and Ca(2) sites that promote a shift of CO_3^{2-} to the A-type location. These cation-dependent carbonate location shifts can in turn modulate the bioapatites mechanical properties [48].

Apatite composition has been shown to significantly affect the crystal mechanics [19, 48, 53]. Here, the mechanical properties of the bioapatite were investigated by examining the response of this material to hydrostatic pressure using synchrotron wide-angle X-ray scattering (WAXS). Bulk modulus was found to remain relatively unchanged as a function of Co and Cr content. We expected that the increased CO_3^{2-}:PO_4^{3-} ratio would lower the bulk modulus [19]; however, it appears that the addition of Co and Cr inhibits the reduction in stiffness. This continues through to the elastic constants as well as the Young's moduli of Co-containing apatites. It had been previously suggested that the modulus of these nano-crystals is controlled by (1) the mineral crystallinity and (2) the bonding strength within the lattice. The addition of CO_3^{2-} and cations like Na^+ and K^+ has indeed been associated with decreased crystallinity and decreased modulus [19, 48], but here, the crystallinity is much more minimally affected. The mechanical properties measured here are only minimally correlated to the FWHM of the c- and a-axis suggesting that they are not regulated by the crystallinity, Table S5. Instead, the mechanical properties are most strongly correlated to c-axis lattice spacing and compositional factors such as cationic concentrations and PO_4^{3-} content (both overall and non-apatitic). This indicates that the small changes in mechanical properties are primarily controlled by the small changes in the lattice spacing affecting bond lengths and therefore bond strengths for Co apatites.

Though the bulk moduli of the Cr apatites are nearly independent of Cr wt% (similar to the Co apatites), increasing Cr wt% substantially decreases the apatite stiffness along the normal axes of loading (dissimilar to the Co apatites). With Cr substitution in the apatites, we see decreasing stiffness along the a- and c-axis with increasing Cr wt%. This can be seen in the low Young's moduli and elastic constants for the apatites with high Cr wt%. Stiffness decreases along the a- and c-axes may be due to electron density distribution differences between hydroxyapatite and the Cr apatites, specifically near the Cr substitution of Ca(2). This can be seen in Fig 8, where bonding between atoms is shown with an isosurface that encompasses the regions with electron density > 0.5 $Å^{-3}$. There is significant shifting of the electron density distribution in the OH^- channel due to Cr substitution; the Cr attracts the nearby O (from OH^- or CO_3^{2-}) in the OH^- channel and thus moves it further from the neighboring Ca(2), Fig 8A. The Cr also attracts O from neighboring PO_4^{3-} and CO_3^{2-}, which causes reorientation of these groups and distortion of the c-axis, Fig 8B. The shift of PO_4^{3-} and CO_3^{2} groups from their locations in hydroxyapatite and resulting electron density distribution change along the c-axis in the Cr apatites results in E_{33} and C_{33} decrease. This has also been noted for Mg and Zn doped hydroxyapatite, in which they also pull O from neighboring PO_4^{3-} and OH^- groups and cause c-axis distortion and C_{33} decrease [70].

In the Cr apatites, covalent bonding between the Cr and the O of OH^- or A-type CO_3^{2-} in the OH^- channel is revealed by shared electron density in the apatites with >3wt% Cr. This is not present in hydroxyapatite, in which there is only ionic bonding between the Ca(2) and OH^-, Fig 8A and Fig 9A. Cr-O bonds are formed in all OH^- channels with Cr substitution of Ca(2), despite the presence of nearby O_i or A-type CO_3^{2-} substitution of the OH^-, Fig 9B and 9C. The covalent Cr-O bonding results in weakening of the ionic bonds between neighboring Ca(2) and OH^- or CO_3^2, as evidenced by electron density decrease between Ca(2) and OH^- or CO_3^{2-} with Cr substitution. Breaking of Ca(2) and OH^- ionic bonds is one of the first failures that occur in hydroxyapatite under tensile loading along the a-axis [71]. Thus, without the strength provided by these ionic bonds in the Cr apatites, there is decreased stiffness along their a-axis, low C_{11}, and low E_{11} values as the Cr substitution wt% increases.

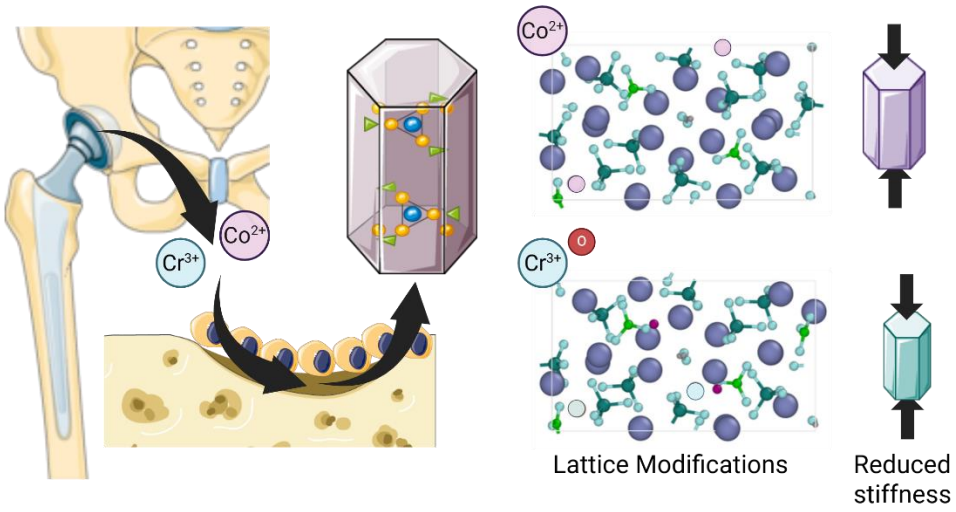


Figure 10: Summary of the proposed process by which Co and Cr ions are released into the boney space. These heavy metal ions are then incorporated into newly formed bone as substitutions in the crystalline phase. Co^{2+} substitutes for Ca^{2+} while Cr^{3+} substitutes for Ca^{2+} alongside an interstitial oxygen. These substitutions modify the lattice spacing and reduce the mineral stiffness especially in the case of Cr^{3+}.

5 Conclusions

Metal-on-metal hip implants are known to release heavy metal ions into the bone environment. This has been associated with systemic toxicity, but little is known about how these heavy metals interact with bone mineral during new bone deposition. Here, apatites containing either Co or Cr were made using aqueous precipitation techniques and characterized. Co and Cr integrated the apatite lattice as Co^{2+} and Cr^{3+} substitutions for Ca^{2+}. Cr^{3+} substitutions required the addition of interstitial oxygens for charge balance. These Co and Cr substitutions induced small modifications to the lattice spacing and crystallinity. These are well predicted by DFT models in which Co and Cr are substituted for Ca. The mechanical properties of the crystals are only minimally affected by the substitution of Co likely due to the small changes in atomic structure. Though the bulk moduli of the

crystals with Cr substitution are also not significantly affected by Cr wt%, formation of covalent Cr-O bonds, resulting weakening of Ca-O ionic bonds, and shifting of PO_4^{3-} and CO_3^{2-} groups cause stiffness decreases along the a- and c-axes in bioapatite with increasing Cr concentration. Overall, this study confirms that Co and Cr can easily integrate into forming bone mineral and that the consequences of those changes are chemically and mechanically significant even if they have minimal structural and bulk mechanical consequences, Fig. 10.

Acknowledgements: This work was supported in part by the Institute of Materials Science at UConn, which provided access to central research facilities and instrumentation. We thank Sobhan Katebifar for collecting the EDX data at CAMMA at UConn. Measurements were performed at PETRA III at DESY (Hamburg, Germany), supported by the Helmholtz Association HGF. The authors gratefully acknowledge beam time on PO7 under proposal I-20231024 and the support of the beamline staff. Funding was provided by NSF grant 107141. KD was supported by the Young Innovative Investigator Program (YIIP) at UConn Health. AN and AE acknowledge support from NSF grant 2434467.

References:

1. Triclot, P., *Metal-on-metal: history, state of the art (2010).* Int Orthop, 2011. **35**(2): p. 201-6.
2. Rieker, C.B., R. Schön, and P. Köttig, *Development and validation of a second-generation metal-on-metal bearing: laboratory studies and analysis of retrievals.* J Arthroplasty, 2004. **19**(8 Suppl 3): p. 5-11.
3. Rieker, C. and P. Kottig, *In vivo tribological performance of 231 metal-on-metal hip articulations.* Hip Int, 2002. **12**(2): p. 73-76.
4. Davis, T.P., *Metal-on-Metal Hip Arthroplasty: A Comprehensive Review of the Current Literature.* Cureus, 2023. **15**(11): p. e48238.
5. Matharu, V.K. and G.S. Matharu, *Metal-on-metal hip replacements: implications for general practice.* Br J Gen Pract, 2017. **67**(665): p. 544-545.
6. Kurtz, S.M., et al., *Prevalence of Metal-on-Metal Bearings in the United States*, in *Metal-On-Metal Total Hip Replacement Devices*. 2013, ASTM International. p. 0.
7. Kovochich, M., et al., *Understanding outcomes and toxicological aspects of second generation metal-on-metal hip implants: a state-of-the-art review.* Crit Rev Toxicol, 2018. **48**(10): p. 853-901.
8. Lohmann, C.H., et al., *Metallic debris from metal-on-metal total hip arthroplasty regulates periprosthetic tissues.* World J Orthop, 2014. **5**(5): p. 660-6.
9. Manfreda, F., et al., *Osteolysis in total hip arthroplasty in relation to metal ion release: Comparison between monolithic prostheses and different modularities.* World J Orthop, 2021. **12**(10): p. 768-780.
10. Sansone, V., D. Pagani, and M. Melato, *The effects on bone cells of metal ions released from orthopaedic implants. A review.* Clin Cases Miner Bone Metab, 2013. **10**(1): p. 34-40.
11. Sabah, S.A., et al., *The risk of cardiac failure following metal-on-metal hip arthroplasty.* Bone Joint J, 2018. **100-b**(1): p. 20-27.
12. Green, B., E. Griffiths, and S. Almond, *Neuropsychiatric symptoms following metal-on-metal implant failure with cobalt and chromium toxicity.* BMC Psychiatry, 2017. **17**(1): p. 33.
13. Rattay, T.W., T. Kluba, and L. Schöls, *Chromium and cobalt intoxication mimicking mitochondriopathy.* Neurological Research and Practice, 2021. **3**(1): p. 40.
14. Chandran, S.E. and N.J. Giori, *Nine-Year Incidence of Kidney Disease in Patients Who Have Had Total Hip Arthroplasty.* The Journal of Arthroplasty, 2011. **26**(6, Supplement): p. 24-27.
15. Cacciotti, I., *Cationic and Anionic Substitutions in Hydroxyapatite*, in *Handbook of Bioceramics and Biocomposites*, I.V. Antoniac, Editor. 2014, Springer International Publishing: Cham. p. 1-68.
16. Wopenka, B. and J.D. Pasteris, *A mineralogical perspective on the apatite in bone.* Materials Science and Engineering: C, 2005. **25**(2): p. 131-143.
17. Gómez-Morales, J., et al., *Progress on the preparation of nanocrystalline apatites and surface characterization: Overview of fundamental and applied aspects.* Progress in Crystal Growth and Characterization of Materials, 2013. **59**(1): p. 1-46.
18. Deymier, A.C., et al., *Protein-free formation of bone-like apatite: New insights into the key role of carbonation.* Biomaterials, 2017. **127**: p. 75-88.
19. Wingender, B., et al., *Carbonate substitution significantly affects the structure and mechanics of carbonated apatites.* Acta Biomaterialia, 2021. **122**: p. 377-386.
20. Tite, T., et al., *Cationic Substitutions in Hydroxyapatite: Current Status of the Derived Biofunctional Effects and Their In Vitro Interrogation Methods.* Materials (Basel), 2018. **11**(11).
21. Wong, S.L., C. Drouet, and A. Deymier, *Carbonate environment changes with Na or K substitution in biomimetic apatites.* Materialia, 2023. **29**: p. 101795.
22. Drake, K.A., et al., *A methodological comparison of synthesizing heavy metal substituted bioapatite.* Methods, 2025. **239**: p. 42-48.
23. Ortali, C., et al., *Consolidation of bone-like apatite bioceramics by spark plasma sintering of*

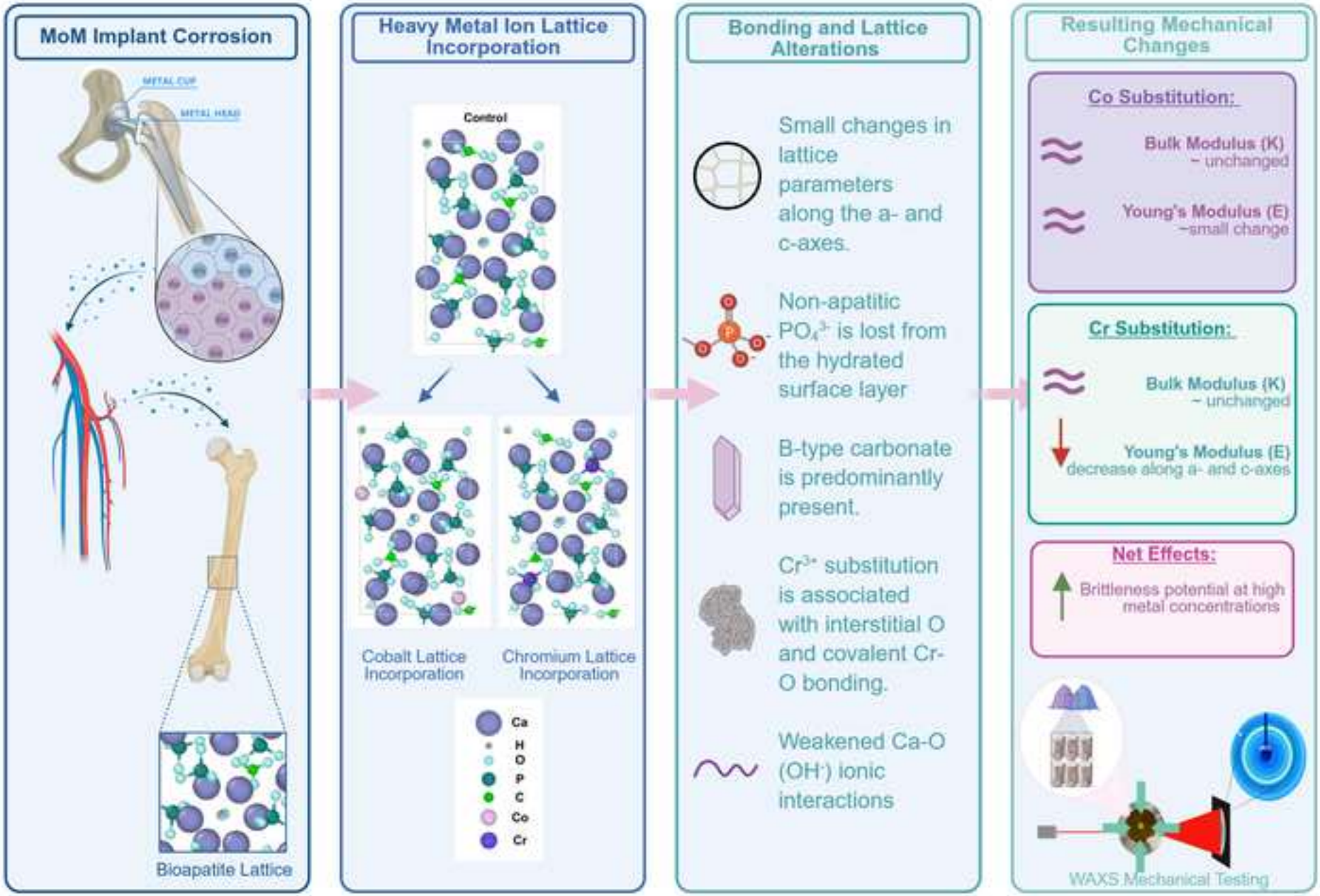
amorphous carbonated calcium phosphate at very low temperature. Journal of the European Ceramic Society, 2018. **38**(4): p. 2098-2109.
24. Ching, W.Y., P. Rulis, and A. Misra, *Ab initio elastic properties and tensile strength of crystalline hydroxyapatite.* Acta Biomaterialia, 2009. **5**(8): p. 3067-3075.
25. Astala, R. and M.J. Stottt, *First-principles study of hydroxyapatite surfaces and water adsorption.* Physical Review B, 2008. **78**(7).
26. Menendez-Proupin, E., et al., *Computer simulation of elastic constants of hydroxyapatite and fluorapatite.* J Mech Behav Biomed Mater, 2011. **4**(7): p. 1011-20.
27. Almora-Barrios, N. and N.H. de Leeuw, *A Density Functional Theory Study of the Interaction of Collagen Peptides with Hydroxyapatite Surfaces.* Langmuir, 2010. **26**(18): p. 14535-14542.
28. Slepko, A. and A.A. Demkov, *First-principles study of the biomineral hydroxyapatite.* Physical Review B, 2011. **84**(13).
29. Mostafa, N.Y. and P.W. Brown, *Computer simulation of stoichiometric hydroxyapatite: Structure and substitutions.* Journal of Physics and Chemistry of Solids, 2007. **68**(3): p. 431-437.
30. Veselinović, L., et al., *Crystal structure of cobalt-substituted calcium hydroxyapatite nanopowders prepared by hydrothermal processing.* Journal of Applied Crystallography, 2010. **43**: p. 320-327.
31. Carrera, K., et al., *Formation of Oxygen Vacancies in Cr3+-Doped Hydroxyapatite Nanofibers and Their Role in Generating Paramagnetism.* Biomedical Materials & Devices, 2025. **3**: p. 529-544.
32. Wakamura, M., K. Kandori, and T. Ishikawa, *Influence of chromium(III) on the formation of calcium hydroxyapatite.* Polyhedron, 1997. **16**(12): p. 2047-2053.
33. Lima, T.A.R.M., et al., *The incorporation of chromium (III) into hydroxyapatite crystals.* Materials Letters, 2015. **140**: p. 187-191.
34. de Araujo, T.S., et al., *Production and characterization of pure and Cr3+-doped hydroxyapatite for biomedical applications as fluorescent probes.* Journal of Materials Science, 2007. **42**: p. 2236-2243.
35. Stukowski, A., *Visualization and analysis of atomistic simulation data with OVITO–the Open Visualization Tool.* Modelling and Simulation in Materials Science and Engineering, 2009. **18**(1): p. 015012.
36. Momma, K. and F. Izumi, *VESTA: a three-dimensional visualization system for electronic and structural analysis.* Journal of Applied Crystallography, 2008. **41**(3): p. 653-658.
37. Giannozzi, P., et al., *QUANTUM ESPRESSO: a modular and open-source software project for quantum simulations of materials.* Journal of Physics: Condensed Matter, 2009. **21**(39): p. 395502.
38. Giannozzi, P., et al., *Advanced capabilities for materials modelling with Quantum ESPRESSO.* Journal of Physics: Condensed Matter, 2017. **29**(46): p. 465901.
39. Vanderbilt, D., *Soft self-consistent pseudopotentials in a generalized eigenvalue formalism.* Physical Review B, 1990. **41**(11): p. 7892-7895.
40. Laasonen, K., et al., *Implementation of ultrasoft pseudopotentials in ab initio molecular dynamics.* Physical Review B, 1991. **43**(8): p. 6796-6799.
41. Laasonen, K., et al., *Car-Parrinello molecular dynamics with Vanderbilt ultrasoft pseudopotentials.* Physical Review B, 1993. **47**(16): p. 10142-10153.
42. Perdew, J.P., K. Burke, and M. Ernzerhof, *Generalized Gradient Approximation Made Simple.* Physical Review Letters, 1996. **77**(18): p. 3865-3868.
43. Grimme, S., *Semiempirical GGA-type density functional constructed with a long-range dispersion correction.* Journal of Computational Chemistry, 2006. **27**(15): p. 1787-1799.
44. Ulian, G. and G. Valdrè, *Second-order elastic constants of hexagonal hydroxylapatite ($P6_3$) from ab initio quantum mechanics: Comparison between DFT functionals and basis sets.* International Journal of Quantum Chemistry, 2018. **118**(5): p. e25500.
45. Peccati, F., et al., *CO_3^{2-} Mobility in Carbonate Apatite As Revealed by Density Functional*

Modeling. The Journal of Physical Chemistry C, 2014. **118**(2): p. 1364-1369.
46. Ulian, G., et al., *Periodic ab initio bulk investigation of hydroxylapatite and type A carbonated apatite with both pseudopotential and all-electron basis sets for calcium atoms.* American Mineralogist, 2013. **98**(2-3): p. 410-416.
47. Ulian, G., et al., *DFT investigation of structural and vibrational properties of type B and mixed A-B carbonated hydroxylapatite.* American Mineralogist, 2014. **99**(1): p. 117-127.
48. Wong, S., et al., *The location of cationic substitutions in carbonated biomimetic apatites significantly affects crystal nanomechanics.* Scientific Reports, 2024. **14**(1): p. 22625.
49. Ren, B., et al., *First principles study of stability, mechanical, and electronic properties of chromium silicides.* Chinese Physics B, 2018. **27**(10): p. 107102.
50. De-Chun, H., et al., *First-principles calculations on phase transition and elastic properties of CoN.* Acta Physica Polonica A, 2016. **130**(3): p. 743-747.
51. Fast, L., et al., *Elastic-Constants of Hexagonal Transition-Metals - Theory.* Physical Review B, 1995. **51**(24): p. 17431-17438.
52. Forien, J.-B., et al., *In situ compressibility of carbonated hydroxyapatite in tooth dentine measured under hydrostatic pressure by high energy X-ray diffraction.* Journal of the Mechanical Behavior of Biomedical Materials, 2015. **50**: p. 171-179.
53. Forien, J.-B., et al., *X-ray diffraction and in situ pressurization of dentine apatite reveals nanocrystal modulus stiffening upon carbonate removal.* Acta Biomaterialia, 2021. **120**: p. 91-103.
54. Krywka, C., et al., *Determination of Silkworm Silk Fibroin Compressibility Using High Hydrostatic Pressure with in Situ X-ray Microdiffraction.* Macromolecules, 2014. **47**(20): p. 7187-7193.
55. Nye, J.F., *Physical properties of crystals: their representation by tensors and matrices*. 1985: Oxford university press.
56. Zolotoyabko, E., *Basic Concepts of Crystallography: An Outcome from Crystal Symmetry*. 2011: Vch Verlagsgesellschaft Verlag GmbH & Company KGaA.
57. Li, Y., *The anisotropic behavior of Poisson's ratio, Young's modulus, and shear modulus in hexagonal materials.* physica status solidi (a), 1976. **38**(1): p. 171-175.
58. Elkabouss, K., et al., *Corrigendum to ?Cobalt-exchanged hydroxyapatite catalysts: magnetic studies, spectroscopic investigations, performance in 2-butanol and ethane oxidative dehydrogenations? [J. Catal. 226 (2004) 16?24].* Journal of Catalysis, 2004. **226**: p. 16-24.
59. Veselinovic, L., et al., *Crystal structure of cobalt-substituted calcium hydroxyapatite nanopowders prepared by hydrothermal processing.* Journal of Applied Crystallography, 2010. **43**(2): p. 320-327.
60. Grisafe, D.A. and F.A. Hummel, *Pentavalent ion substitutions in the apatite structure part A. Crystal chemistry.* Journal of Solid State Chemistry, 1970. **2**(2): p. 160-166.
61. Banks, E. and K.L. Jaunarajs, *Chromium Analogs of Apatite and Spodiosite.* Inorganic Chemistry, 1965. **4**(1): p. 78-83.
62. Sallam, S.M., et al., *Synthesis and characterization of hydroxyapatite contain chromium.* Journal of Biophysical Chemistry, 2012. **3**: p. 278-282.
63. Carrera, K., et al., *Formation of Oxygen Vacancies in Cr3+-Doped Hydroxyapatite Nanofibers and Their Role in Generating Paramagnetism.* Biomedical Materials & Devices, 2025. **3**(1): p. 529-544.
64. de Araujo, T.S., et al., *Production and characterization of pure and Cr3+-doped hydroxyapatite for biomedical applications as fluorescent probes.* Journal of Materials Science, 2007. **42**(7): p. 2236-2243.
65. McConnell, D., *Deficiency of phosphate ions in apatite.* Naturwissenschaften, 1965. **52**(8): p. 183-183.
66. Mabilleau, G., et al., *Cobalt, chromium and nickel affect hydroxyapatite crystal growth in vitro.* Acta Biomater, 2010. **6**(4): p. 1555-60.
67. Baig, A.A., et al., *Effect of Carbonate Content and Crystallinity on the Metastable Equilibrium Solubility Behavior of Carbonated Apatites.* Journal of Colloid and Interface

Science, 1996. **179**(2): p. 608-617.
68. Baig, A.A., et al., *Relationships Among Carbonated Apatite Solubility, Crystallite Size, and Microstrain Parameters.* Calcified Tissue International, 1999. **64**(5): p. 437-449.
69. Nelson, D.G.A., *The Influence of Carbonate on the Atomic Structure and Reactivity of Hydroxyapatite.* Journal of Dental Research, 1981. **60**(C): p. 1621-1629.
70. Aryal, S., K. Matsunaga, and W.-Y. Ching, *Ab initio simulation of elastic and mechanical properties of Zn- and Mg-doped hydroxyapatite (HAP).* Journal of the Mechanical Behavior of Biomedical Materials, 2015. **47**: p. 135-146.
71. Snyder, A.D. and I. Salehinia, *Study of nanoscale deformation mechanisms in bulk hexagonal hydroxyapatite under uniaxial loading using molecular dynamics.* Journal of the Mechanical Behavior of Biomedical Materials, 2020. **110**: p. 103894.

Graphical Abstract

Click here to access/download;Graphical Abstract;Graphical abstract.jpeg



Click here to access/download
Electronic Supplementary Material
260803_Co-Cr-Supplemental Figures.pptx

Response to Reviewers with images

Click here to access/download
Electronic Supplementary Material
260803_Response to Reviewers_Final.docx